

pubs.acs.org/JPCB Article

Fluorescence Anisotropy Decays and Microscale-Volume Viscometry Reveal the Compaction of Ribosome-Bound Nascent Proteins

Rachel B. Hutchinson, Xi Chen, Ningkun Zhou, and Silvia Cavagnero*



Cite This: J. Phys. Chem. B 2021, 125, 6543-6558



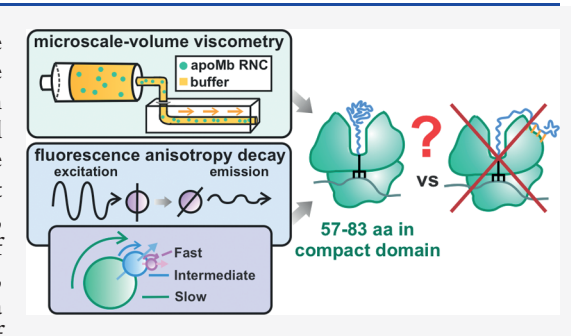
ACCESS I

Metrics & More

Article Recommendations

Supporting Information

ABSTRACT: This work introduces a technology that combines fluorescence anisotropy decay with microscale-volume viscometry to investigate the compaction and dynamics of ribosome-bound nascent proteins. Protein folding in the cell, especially when nascent chains emerge from the ribosomal tunnel, is poorly understood. Previous investigations based on fluorescence anisotropy decay determined that a portion of the ribosome-bound nascent protein apomyoglobin (apoMb) forms a compact structure. This work, however, could not assess the size of the compact region. The combination of fluorescence anisotropy with microscale-volume viscometry, presented here, enables identifying the size of compact nascent-chain subdomains using a single fluorophore label. Our results demonstrate that the compact region of



nascent apoMb contains 57–83 amino acids and lacks residues corresponding to the two native C-terminal helices. These amino acids are necessary for fully burying the nonpolar residues in the native structure, yet they are not available for folding before ribosome release. Therefore, apoMb requires a significant degree of post-translational folding for the generation of its native structure. In summary, the combination of fluorescence anisotropy decay and microscale-volume viscometry is a powerful approach to determine the size of independently tumbling compact regions of biomolecules. This technology is of general applicability to compact macromolecules linked to larger frameworks.

■ INTRODUCTION

Correct protein folding is essential for the proper function of living organisms and for the efficient large-scale production of biomedically relevant proteins in the context of biotechnology and pharmaceutical applications. While *in vitro* refolding of pure proteins has helped explain general aspects of the process and underlying trends, ^{1–3} protein folding within the cellular environment, including the role of the ribosome and molecular chaperones, is still poorly understood. ^{4–7}

Many proteins begin folding cotranslationally before they are released from the ribosome. 4,8-15 The ribosome plays an important role in protein folding. On the one hand, it may act as a chaperone. On the other hand, the ribosome is known to influence cotranslational folding by confining the motion of nascent chains, 9,15,22,23 by enabling interactions between the nascent chain and the ribosomal tunnel and (or) ribosomal surface 46-29 and by promoting nascent-chain solubility. Immediately after release from the ribosome, single-domain nascent proteins must be properly kinetically channeled to their native state to prevent the formation of aggregated states. The ribosomal exit tunnel, which is approximately 100 Å long and has a width of 10-20 Å, can be divided into two regions: the tunnel core and the vestibule, which encompasses the last 20 Å of the tunnel and is wider than the rest of the ribosomal tunnel. The exit tunnel generally hosts approximately 30-40 amino acids, depending on the sequence and structure of the nascent protein. 23,33-38

More residues can be hosted if the nascent protein adopts the tertiary structure within the tunnel. The tunnel structure within the tunnel structure, nascent chains can form an α -helical secondary structure, 9,23,38,39 tertiary interactions, 10,40 and even fully folded states. 36,37,41 In addition, larger tertiary structures can form within the tunnel vestibule. 12,42,43

In order to better understand the extent of protein folding during protein biogenesis, Ellis et al. addressed the development of nascent-protein compaction within stalled ribosome-bound nascent chains (RNCs). The protein apomyoglobin from sperm whale (apoMb) was selected as a model system for this work, and transcription—translation was carried out in cell-free systems. These studies addressed RNC compaction as a function of chain elongation by fluorescence anisotropy-decay analysis. The investigations by Ellis et al. revealed two rotational motions of short nascent chains (less than 57 amino acids) that correspond solely to the dynamics of the ribosome and the fluorescently labeled N-terminal region of the nascent chain. However, apoMb RNCs bearing nascent chains longer

Received: May 20, 2021 **Revised:** May 26, 2021 **Published:** June 10, 2021





than 57 residues also display a third motion corresponding to a rotational correlation time of several nanoseconds. This dynamic component is absent from the anisotropy decay of RNCs carrying an intrinsically disordered nascent protein, and it is characterized by a smaller rotational correlation time (ca. 5–9 ns) than the ribosome-released folded protein (ca. 40–50 ns). This anisotropy-decay component established the presence of a compact subdomain within the nascent chain. ¹³

The abovementioned investigations, however, were unable to unequivocally determine the number of amino acids belonging to the compact nascent-chain domain, given that they relied on indirect information on solution viscosity inferred from fluorescence data. Specifically, the abovementioned studies estimated the viscosity of RNC solutions from the rotational correlation time of either a small fluorescent dye or ribosome-released apoMb. 13 Given that the solution viscosity deduced from these two approaches were significantly different, it was impossible to draw clear conclusions on the size of the compact RNC subdomain. Therefore, while previous work demonstrated that RNCs longer than 57 residues bear a compact nascent chain, the number of amino acids corresponding to this compact region could not be assessed. This concept is pictorially illustrated in Figure 1, which shows that conformations a-c can be excluded due to previous studies reporting small-amplitude local RNC motions on the nanosecond time scale. 13 Until now, however, it has been impossible to discriminate between small (species d) and large (species e and f) nascent-chain conformations.

In this work, we address the abovementioned gap of knowledge by combining fluorescence anisotropy decays with direct viscosity measurements to identify the size of compact nascent-chain domains of apoMb RNCs. Our results show that the compact nascent chain comprises 37-54% of the amino acid sequence; hence, it lacks C-terminal residues corresponding to 46-63% of the chain. Therefore, a significant portion of the RNC must fold post-translationally. In all, this work demonstrates that fluorescence anisotropy decays can be synergistically combined with microscale-volume viscometry to unveil the size and compaction of nascent-chain regions. The technology introduced here is of wide applicability to any compact macromolecule linked to larger frameworks. In addition, this approach is particularly straightforward as it only requires a single fluorophore (extrinsic or intrinsic) per biomolecule of interest.

METHODS

Generation of RNC Complexes. An Escherichia coli cellfree transcription-translation system was used to produce apoMb₁₅₃ RNC complexes as described. 13,45 This cell-free system included an E. coli S30 extract prepared from the K12 A19 strain 45,46 and a pET-Blue1 plasmid encoding the spermwhale apomyoglobin gene with an E. coli-optimized nucleotide sequence.⁴⁷ In addition, the cell-free system included oligodeoxynucleotides designed to carry a complementary sequence to that of the mRNA region immediately before the stop codon (see the Supporting Information for more details). Consistent with the oligodeoxynucleotide-directed mRNA cleavage approach,4 the oligodeoxynucleotides bind the mRNA, followed by site-specific DNA-RNA-hybrid cleavage by endogenous RNaseH. 48 The resulting stalled RNC complex carried the full-length apoMb protein. An anti-SsrA oligodeoxynucleotide was added to the cell-free system to prevent tmRNA-mediated release of nascent proteins from the

Limiting models for ribosome-bound nascent chain (RNC) compaction and size

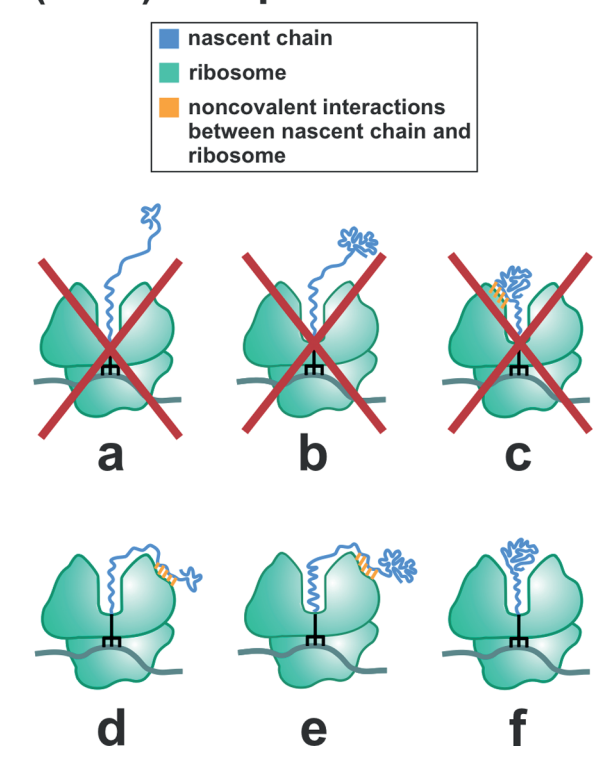


Figure 1. Hypothetical limiting models describing the ribosome-bound apoMb nascent-chain compaction. Models a and b can be eliminated due to the known highly spatially confined environment of the nascent chain (cone semiangle = $20 \pm 1^{\circ}$). Model c can be eliminated because the compact region explored in this work independently tumbles on the low-nanosecond time scale (see fluorescence anisotropy-decay analysis). This time scale is incompatible with the much slower tumbling of the ribosome. Models d, e, and f are consistent with previously published work but could not be discriminated from each other in the past.

ribosome.⁴⁹ The N-terminal methionine was labeled with BODIPY-FL using BODIPY-FL Met-tRNA^{fMet}, which was prepared and added to the cell-free system as described.¹³ Cell-free components were assembled at room temperature (0.75–1.05 mL total volume) followed by splitting into 75 μ L of equivolume aliquots and parallel incubation of all aliquots at 37 °C for 30 min.

Purification of RNC Complexes. After cell-free transcription—translation, RNC complexes were purified upon centrifugation (160,000 rcf for 60 min at 4 °C) of each of the aliquots over a 150 μ L of sucrose cushion (1.1 M sucrose, 20 mM tris—HCl, 10 mM Mg²⁺ acetate, 500 mM NH₄Cl, 0.5 mM EDTA, and 1 mM DL-dithiothreitol, pH adjusted to 7.0). Pellets containing RNC complexes were then solubilized in 15 μ L of resuspension buffer (10 mM Tris HCl, 10 mM Mg(OAc)₂, 60 mM NH₄Cl, 0.5 mM EDTA, and 1 mM dithiothreitol, pH 7.0). All 15 μ L aliquots were then combined, mixed, and then further split for anisotropy-decay and viscosity data collection, which were run in parallel each day. The ribosome-bound status of the nascent chains was verified via a puromycin assay (see the Supporting Information for details and representative SDS-PAGE data) performed on the same

samples previously subjected to fluorescence measurements. 51,52

Concentration of Purified RNCs. The total ribosome concentration of resuspended RNCs was assessed from sample absorbances at 260 nm, considering the extinction coefficient of the 70S *E. coli* ribosome (3.91 × 10⁷ M⁻¹ s⁻¹).⁵³ The concentration of BODIPY-FL-labeled RNCs was determined from the fluorescence intensity of RNC gel bands, upon comparison with the fluorescence intensity of reference gel bands of BODIPY-FL Met-tRNA^{fMet} of known concentration. ApoMb gel band intensities were determined with the ImageJ software. ^{34,55}

Fluorescence Anisotropy Decay: Data Collection and Analysis. Fluorescence anisotropy-decay data were collected with a Chronos frequency-domain fluorometer (ISS Inc.). Samples were excited at 477 nm with a laser diode. A 480 \pm 5 nm band-pass filter was used for the excitation channel and a 520 \pm 20 nm band-pass filter (Chroma Technology) was used for the emission channel. The excitation polarizer was set vertical for lifetime and anisotropy measurements. The emission polarizer was set to 54.7° for lifetime measurements. Samples were incubated at 25 °C for at least 30 min prior to fluorescence measurements. Sample temperature was maintained at 25 \pm 0.1 °C during fluorescence measurements with a circulating water bath.

Lifetime and anisotropy-decay data were analyzed with the Globals software package (Laboratory for Fluorescence Dynamics, LFD).⁵⁶ The standard deviation for phase and modulation was set to 0.2° and 0.004, respectively, to estimate reduced χ^2 values.⁵⁷ Lifetime data were fit to three discrete exponential decay components, one of which was fixed to 1 ps to account for light scattering, and the other two, corresponding to the actual fluorophore lifetimes, were allowed to float. Anisotropy data were corrected taking the experimental frequency-dependent G-factor into account. The latter parameter was determined on the same day as the anisotropy-decay measurements. Then, anisotropy data were then fit to multiexponential decays. The fundamental anisotropy r_0 was fixed at 0.37. In order to assess best fits, all data were independently fit to both two- and threecomponent decays and χ^2 values were compared. Threecomponent fits were chosen if their χ^2 values were $\leq 2.5 \times$ smaller than the χ^2 values for two-component fit. The number of amino acids in the compact domain of the nascent protein was determined upon evaluating both spherical and prolate (representative axial ratio = 3.5) and oblate (representative axial ratio = 0.5) ellipsoid models. Order parameters and cone semiangles were determined as described. ÎS See the Supporting Information for further details on χ^2 and compact-domain calculations. Anisotropy-decay simulations were performed with the Vinci software (ISS, Inc.).

Derivation of Equations Used for Ellipsoidal Models. Spherical, prolate ellipsoidal, and oblate ellipsoidal models were used to calculate the number of amino acids contained in the compact subdomain of the nascent protein. We used ellipsoids of revolution for the ellipsoid models, which have two axes with equivalent length (Figure 8). These ellipsoids can have three different rotational correlation times, but these three correlation times are nearly identical for oblate ellipsoids and prolate ellipsoids with an axial ratio less than five and are too close to be resolved via our method. S8,59 Therefore, for the ellipsoidal models, the harmonic-mean rotational correlation time $\tau_{\rm H}$ was used and determined according to 60

$$\tau_{\rm H} = \left(\frac{0.4}{\tau_1} + \frac{0.4}{\tau_2} + \frac{0.2}{\tau_3}\right)^{-1} \tag{1}$$

where τ_1 , τ_2 , and τ_3 were determined from the parallel and perpendicular components of the rotational diffusion coefficient according to

$$\tau_{1} = (D_{\parallel} + 5D_{\perp})^{-1} \tag{2}$$

$$\tau_2 = (4D_{||} + 2D_{\perp})^{-1} \tag{3}$$

$$\tau_3 = (6D_{\perp})^{-1} \tag{4}$$

Substituting eqs 2-4 into eq 1 gives

$$\tau_{\rm H} = (0.4(D_{\parallel} + 5D_{\perp}) + 0.4(4D_{\parallel} + 2D_{\perp}) + 0.2(6D_{\perp}))^{-1}$$
(5)

which simplifies to

$$\tau_{\rm H} = (2D_{\parallel} + 4D_{\perp})^{-1} \tag{6}$$

 D_{\parallel} and D_{\perp} are defined as

$$D_{\parallel} = \left(\frac{3\rho(\rho - b)}{2(\rho^2 - 1)}\right) D_{\text{sphere}}$$
(7)

$$D_{\perp} = \left(\frac{3\rho[(2\rho^2 - 1)b - \rho)]}{2(\rho^4 - 1)}\right) D_{\text{sphere}}$$
(8)

where ρ is the aspect ratio and b is defined as

$$b = (\rho^2 - 1)^{-1/2} \ln[\rho + (\rho^2 - 1)^{1/2}]$$
 for prolate ellipsoids (9)

$$b = (1 - \rho^2)^{-1/2} \arctan \left[\frac{(1 - \rho^2)^{1/2}}{\rho} \right]$$

Viscosity Measurements. The viscosity of apoMb RNC solutions was measured with a microVISC viscometer (Rheosense, Inc.), an apparatus tailored to small-volume samples (15–60 μ L depending on shear rate). Samples were allowed to flow through the viscometer channel at a constant shear rate, and pressure differences as the fluid flow within the channel were measured, to assess sample viscosity. The viscosity of apoMb RNC solutions was determined at shear rates 1500, 3000, 5000, 6500, and 8000 s⁻¹, with a temperature-control module set to 25 °C. Viscosity measurements with an R^2 value lower than 0.995 were discarded. Plots of viscosity versus shear rate and student's t-test calculations were used to compare viscosity values. This analysis let us to conclude that all samples analyzed in this work exhibit Newtonian behavior.

Fluorescence-Detected Gel Electrophoresis. SDS-PAGE via three-layer tris-tricine low-pH gels⁶¹ was employed to analyze RNCs in the absence and presence of puromycin. Fluorophore-labeled peptidyl tRNAs (carrying nascent proteins) were visualized directly on the gels with an FLA 9500 Typhoon Gel Imager (GE Healthcare Life Sciences), 473 nm excitation laser, and BPB1 emission filter (525/50 nm band-pass filter).

RESULTS AND DISCUSSION

Experimental Design. This study employs apoMb as a model system. The holo form of this protein, containing the heme cofactor, occupies a special place in chemistry and biology as it was the very first protein whose structure was solved by X-ray crystallography. In addition, apoMb carries the ubiquitous all- α -helical globin fold. and its *in vitro* refolding mechanism was extensively characterized via classical refolding experiments from a denaturant as well as within cell-relevant environments. 13,15,30,45,73 The apoMb plasmid is codon-usage-optimized for expression in *E. coli.* The spombol of the coling is codon-usage-optimized for expression in *E. coli.* The spombol of the coling is a model of the coling is a model of the coling is codon-usage-optimized for expression in *E. coli.* The spombol of the coling is codon-usage-optimized for expression in *E. coli.* The coling is a model of the coling is codon-usage-optimized for expression in *E. coli.* The coling is a model of the coling is codon-usage-optimized for expression in *E. coli.* The coling is a model of the coling is codon-usage-optimized for expression in *E. coli.* The coling is codon-usage-optimized for expression in *E. coli.* The coling is codon-usage-optimized for expression in *E. coli.* The coling is codon-usage-optimized for expression in *E. coli.* The coling is codon-usage-optimized for expression in *E. coli.* The coling is codon-usage-optimized for expression in *E. coli.* The coling is codon-usage-optimized for expression in *E. coli.* The coling is codon-usage-optimized for expression in *E. coli.* The coling is codon-usage-optimized for expression in *E. coli.* The coling is codon-usage-optimized for expression in *E. coli.* The coling is codon-usage-optimized for expression in *E. coli.* The coling is codon-usage-optimized for expression in *E. coli.* The coling is codon-usage-optimized for expression in *E. coli.* The coling is codon-usage-optimized for expression in *E. coli.* The coling is codon-usage-optimized for expr

To explore the compaction and dynamics of apoMb in a cell-relevant environment, we generated stalled full-length RNCs of this protein in an *E. coli* cell-free system. The N-terminal methionine was labeled with the fluorophore BODIPY-FL. Ribosomes harboring nascent protein chains were purified and resuspended in a buffer solution to remove free fluorophore, tRNA, and released protein from the solution before performing fluorescence anisotropy-decay and viscosity measurements. We verified that the nascent chain was bound to the ribosome with a puromycin assay, after completing the fluorescence anisotropy decay and viscosity measurements (supporting Figure S1).

The overall experimental design is schematically illustrated in Figure 2. Briefly, we assessed fluorescence anisotropy decays in the frequency domain 58,74 and combined this technique with direct microscale-volume viscosity measurements on the same samples. In this way, we could determine the number of amino acids contained in the compact portion of the nascent chain. The rotational correlation time (τ_c) of a molecular system of interest depends on its size (e.g., its number of amino acids, #aa), shape, and solution viscosity (η) . Therefore, the $\tau_{\rm c}$ of the nascent chain was determined via fluorescence anisotropy decay and the η was assessed with a microscalevolume viscometer. Then, we employed the Stokes-Einstein Debye equation to determine the hydrated volume (V_h) of the compact domain of the nascent chain from experimental rotational correlation time and solution viscosity values, assuming spherical and prolate or oblate ellipsoidal shapes of representative aspect ratios $\rho = 3.5$ or $\rho = 0.5$, respectively. We then calculated the number of amino acids (# aa) from the volume (V_h) considering that the standard protein dry volume of 0.75 mL/g includes 0.2 mL of water per g of protein⁶⁰ and the average molecular weight of amino acids is 110 g/mol.

Combining Anisotropy Decay with Microscale-Volume Viscometry is a Convenient Approach to Determine the Size of Independently Tumbling Compact Regions of Biomolecules, Including RNCs. Fluorescence anisotropy decay and microscale-volume viscometry can be synergistically combined to determine the size and dynamics of compact independently tumbling regions of biomolecules. This method is nonperturbative and can be used to study both compaction and dynamics of nascent proteins in solution. Our approach does not need extrinsic SecM sequences to stall translation and is particularly convenient because it only requires a single fluorophore, making it easily applicable to any protein of interest. We attached the fluorophore to the protein N-terminus, but the fluorescent label can be located anywhere on the independently tumbling region of the macromolecule where it does not interact with immobilized or slowly tumbling species.

Workflow design **Experimental data** 1. measure τ by fluorescence anisotropy decay 2. measure η by microscale-volume viscometry Size determination of compact macromolecules Spherical model $eq. 1 \rightarrow D_{sphere} \xrightarrow{eq. 2} V_h \xrightarrow{eq. 3} # aa$ Ellipsoidal model $\tau_{_{N}} \xrightarrow{\text{eq. 4}} D_{_{\text{sphere}}} \xrightarrow{\text{eq. 2}} V_{_{h}} \xrightarrow{\text{eq. 3}} \# \text{ aa}$ eq. 4: $\tau_h = (2D_s + 4D_\perp)^{-1} = \left[\left(\frac{3\rho(\rho - b)}{(\rho^2 - 1)} \right) D_{sphere} + \left(\frac{6\rho[(2\rho^2 - 1)b - \rho]}{(\rho^4 - 1)} \right) D_{sphere} \right]$ and Methods for derivation of eq. 4 Prolate ellipsoids: eq. 5: b = $(\rho^2 - 1)^{-1/2} \ln [\rho + (\rho^2 - 1)^{1/2}]$; Oblate ellipsoids: eq. 6: b = $(1 - \rho^2)^{-1/2}$ arctan $\left[\frac{(1 - \rho^2)^{1/2}}{2} \right]$ ρ = 0.5 = rotational correlation time = viscosity = harmonic mean correlation time = hydrated peptide volume = rotational diffusion coefficient (sphere) = ellipsoid axial ratio = parallel rotational diffusion = Avogadro's number coefficient (ellipsoid) = hydrated protein density d = perpendicular rotational diffusion MW₋₋ = average amino acid coefficient (ellipsoid) molecular weight

Figure 2. Summary of workflow design to determine the degree of compaction of RNCs. The rotational correlation time $(\tau_{\rm c})$ describing nascent-chain compact-subdomain motions and RNC macroscopic viscosity $(\eta_{\rm macro})$ were determined via fluorescence anisotropy decay in the frequency domain and microscale-volume viscometry, respectively. Experimentally determined values were employed to determine the size of the compact subdomain. Spherical, prolate ellipsoidal, and oblate ellipsoidal models were used to model the compact region of the nascent chain.

= constant for ellipsoid model

= universal gas constant

Fluorescence anisotropy decay alone has been previously used to study conformation and dynamics of biomolecules such as foldable and intrinsically disordered proteins, nucleic acids, the actin—myosin system, and antibodies. Fluorescence anisotropy decay can be used to resolve local and global dynamics not only in nascent—protein—ribosome complexes but also in ribosome-released foldable and intrinsically disordered proteins and in protein fibrils.

The method introduced here is versatile because it can be straightforwardly applied to any complex biomolecule containing an independently tumbling compact region.

Viscosity Measurements and Newtonian Versus Non-Newtonian Fluids. The rotational correlation time of a molecule depends on its size and solution viscosity, as shown in Figure 2. Therefore, viscosity measurements are required to determine the size of compact domains of RNCs. Here, we solve this challenge by performing direct solution viscosity measurements in situ. As shown in the sections below, we also took into account how shear rate, molecular crowding, and the highly negatively charged surface of the ribosome may affect the local viscosity in proximity of the nascent protein surface.

= number of amino acids

in compact region

Solution viscosity may depend on the shear rate (i.e., the flow rate) of the fluid of interest. Newtonian fluids have a constant viscosity that is not affected by shear rate. Non-Newtonian fluids include shear-thinning fluids, which undergo a decrease in viscosity as shear rate increases, and shearthickening solutions, which experience an increase in viscosity as shear rate increases.⁸² Many fluids show Newtonian behavior at low shear rates and then Non-Newtonian behavior at higher shear rates. 83–85 However, several globular proteins including globulins, especially bovine globulin serum albumin, ovalbumin, and β -lactoglobulin, display shear-thinning behavior at low shear rates and Newtonian behavior at higher shear rates. 86-91 For these proteins, shear-thinning behavior occurs at low shear rates (less than 100 s⁻¹) because the proteins form a film at the liquid-gas interface. Within this film, the solution is viscoelastic and experiences a higher viscosity compared to the experimentally measured macroscopic viscosity η_{macro} . As the shear rate increases, the increased flow breaks up the film, decreasing the solution viscosity. Nonglobulin proteins, E. coli ribosomes, mixtures of RNA and proteins, 4 and DNA solutions, 95,96 on the other hand, show Newtonian behavior at low shear rates. In order to assess whether a given solution displays Newtonian or non-Newtonian behavior, it is necessary to perform experimental measurements at different shear rates.

Effect of Molecular Crowding and Excluded Volume on Viscosity. The Stokes–Einstein (SE) and Stokes–Einstein–Debye (SED) relations (see eqs 11 and 12 below, respectively) show how a particle's translational ($D_{\rm t}$) and rotational ($D_{\rm r,sphere}$) diffusion depend on solution viscosity

$$D_{\rm t} = \frac{k_{\rm B}T}{6\pi\eta r} \tag{11}$$

$$D_{\rm r,sphere} = \frac{k_{\rm B}T}{8\pi\eta r^3} = \frac{RT}{6\eta V_{\rm h}} \tag{12}$$

where $k_{\rm B}$ is the Boltzmann constant, T is the temperature in kelvin, η is the solution viscosity, r is the radius of the particle, $V_{\rm b}$ is the hydrated volume of the molecule of interest, and R is the universal gas constant. The abovementioned equations assume homogeneous solution viscosity and noninteracting spherical particles. Within physiologically relevant systems, however, molecular crowding may cause experimental diffusion coefficients to differ from the values predicted from experimental macroscopic viscosity ($\eta_{\rm macro}$) and the SE and SED equations (eqs 11 and 12). ^{97–101} Both negative and positive deviations, leading to faster and slower experimental diffusion than predicted from eqs 11 and 12, respectively, were observed to date. Negative deviations were observed for protein translational and rotational diffusion in the presence of polymer 102–105 and selected protein 106 crowders. This solution behavior was predicted using a Brownian dynamics model. 107 This negative deviation from the SE and SED equations can be explained by the excluded volume effect. The space unavailable to a molecule, known as the excluded volume, includes the space occupied by other molecules and a depletion layer, which is the region surrounding a particle that is depleted in other particles compared to the bulk solution (Figure 3). 108-110 Given that the depletion layer is inaccessible to crowder molecules, the viscosity within this space, denoted as $\eta_{\rm dl}$, is lower than $\eta_{\rm macro}$ and approaches the pure solvent viscosity $\eta_{\rm s}$. In summary, $\eta_{\rm s} \leq \eta_{\rm dl} \leq \eta_{\rm macro}$ (Figure 3c). When $\eta_{\rm dl}$ is less than $\eta_{\rm macro}$, both translational and

Molecular crowding and viscosity

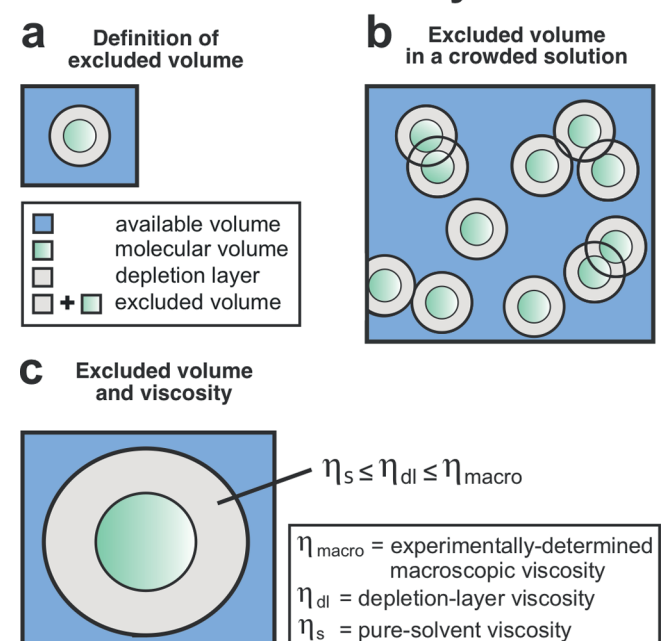


Figure 3. Effect of molecular crowding and excluded volume on microscale-volume viscosity. (a) Excluded volume comprises the space occupied by molecules (green) and the depletion layer surrounding them (gray). (b) Within a crowded solution, two molecules cannot occupy the same space, but their depletion layers can overlap. (c) Viscosity within the depletion layer ($\eta_{\rm dl}$) surrounding a particle is between the pure-buffer (solvent system) viscosity ($\eta_{\rm s}$) and the experimentally measured macroscopic viscosity ($\eta_{\rm macro}$).

rotational diffusion can be faster than the diffusion behavior predicted from eqs 11 and 12. The deviation for rotational diffusion, however, is greater because rotational tumbling occurs entirely within the depletion layer. 100,101

In the case of most protein crowders, however, experimental results⁹⁷ and molecular dynamics simulations¹¹¹ show positive deviations. These results are explained by transient cluster formation between proteins, which becomes significant at high protein concentration (>100 mg/mL) and increases the apparent radius of the rotating species, thus slowing down translational and rotational diffusion.^{97,111} In these concentrated protein solutions, the effect of transient associative interactions counteracts the effect of the depletion layer.

In our experiments, we employed a BODIPY-FL labeled RNC concentrations of ca. 0.1 mg/mL (40 nM) and total ribosome concentrations of ca. 2 mg/mL (790 nM). See the Methods section for procedures employed to determine RNC concentrations. Given that these values are significantly lower than 100 mg/mL, we do not expect clustering to play a significant role.

Effect of Charge on Viscosity. The local environment of the nascent chain is affected by the presence of the ribosome. The ribosomal RNA and charge segregation of ribosomal proteins 112 render the ribosomal surface highly negatively charged, with a formal charge of nearly -4000 per ribosome. 32,113 In general, the charge of polyelectrolytes alters solution characteristics relative to solutions of uncharged polyelectrolytes. This phenomenon is known as the "poly-

electrolyte effect."^{114,115} Specifically, the negative surface charge of the ribosome ^{32,112,113} is likely surrounded by a high-density mostly positively charged counterion layer, based on model studies on RNA and proteins. ¹¹⁶ The Coulombic interactions between the counterion layer and negatively charged ribosome surface shield repulsive interactions. ^{112,116} Therefore, given that the environment surrounding ribosome-bound nascent proteins has a higher ion concentration than the surrounding solution, we asked whether this environment could affect the local viscosity experienced by the nascent chain.

Under high-salt solution conditions relevant to our work (0.1-1 M), the experimental viscosity of highly charged negatively or positively electrolytes approaches the viscosity of the buffer (i.e., the same solution lacking the electrolytes). Therefore, we measured the viscosity of the buffer system (η_s , i.e., our solution lacking RNCs) in addition to the viscosity of the RNCs in buffer (η_{macro}) to assess the effect of charge on the local viscosity near the surface of the ribosome.

Experimental Viscosity of apoMb RNC Solutions. The viscosities of apoMb RNC solutions at shear rates ranging from $1500 \text{ to } 8000 \text{ s}^{-1}$ were not statistically different, according to the two-tailed Student *t*-test (Figure 4 and supporting Table

Experimentally-determined viscosity of apoMb₁₅₃ RNC solutions

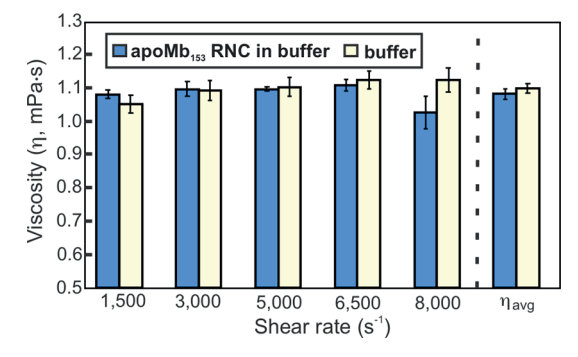


Figure 4. Experimentally measured viscosity of RNC solutions (blue) and buffer (yellow).

S1). This result demonstrates that the apoMb RNC solution behaves as a Newtonian fluid over the tested shear-rate range. We could not directly measure the viscosity at shear rates lower than 1500 s⁻¹ due to the limitations of the microscale-volume viscometer. However, we expect RNC solutions to also show Newtonian behavior at lower shear rates because most fluids including DNA, nonglobulin proteins, and ribosomes in aqueous solutions show Newtonian behavior at low shear rates. ^{83–85,92–96} It is worth mentioning that some globulin and albumin protein solutions display shear-thinning behavior at low shear rates due to their tendency to bind other molecules and form a film at the air—water surface interface. ^{86–91} We expect our RNC samples, however, to show Newtonian behavior at low shear rates because previous work revealed that ribosome solutions are Newtonian fluids at low shear rates. ⁹³

Regarding the potential effect of transient clustering (i.e., nonspecific macromolecular interactions), we expect it to be negligible because the total ribosome concentration in our

samples (ca. 2 mg/mL) is significantly lower than the concentration required for significant clustering (>100 mg/mL). We considered the effects of the depletion layer and charge on local viscosity by comparing $\eta_{\rm macro}$ of the RNC solution with the pure buffer viscosity (η_s). For our sample, η_s (1.10 \pm 0.06 mPa·s) is the same within error as $\eta_{\rm macro}$ for the RNC solution (1.08 \pm 0.02 mPa·s) (Figure 4 and supporting Table S2). These viscosity values are close to the previously reported value of 0.94 \pm 0.02 mPa·s for ribosome solutions. Given that $\eta_{\rm macro}$ and η_s are identical within error, we determined that the effective rotational viscosity is the same as the $\eta_{\rm macro}$ measured via microscale-volume viscometry.

In conclusion, the viscosity of our RNC solutions is not significantly affected by depletion layer, clustering, or charge effects. Therefore, the experimentally measured RNC solution viscosity ($\eta_{\rm macro}$) over all tested shear rates was used to assess the number of amino acids corresponding to the nascent-chain compact subdomain.

Fluorescence Anisotropy Decays Are an Effective Probe of Rotational Dynamics. During anisotropy measurements, a sample labeled with a fluorescent molecule is irradiated with polarized light, which preferentially excites fluorophores with transition dipoles aligned with the electric field of the incoming light. Solution of the fluorophores while in the excited state results in a depolarization of the emitted light compared to the excitation light. The degree of depolarization can be described quantitatively by fluorescence anisotropy, which is defined as

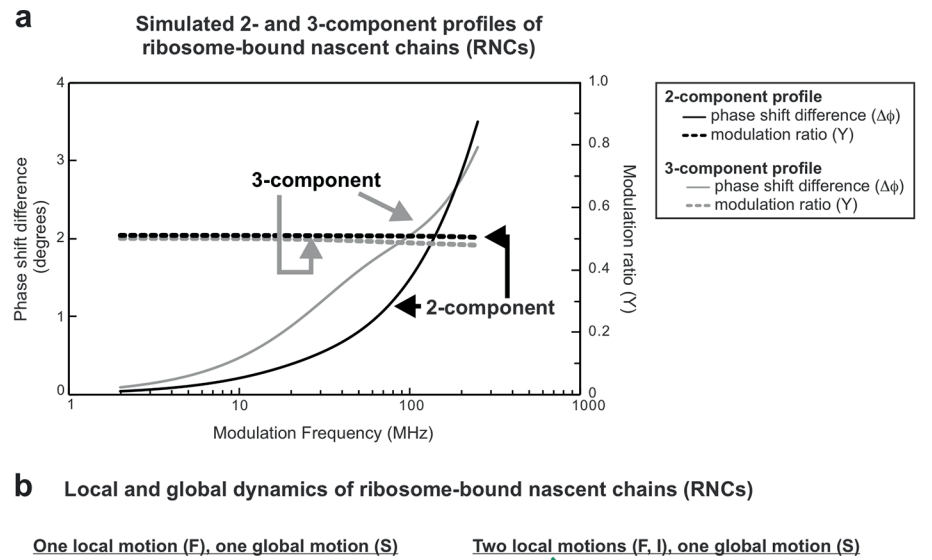
$$r = \frac{I_{\parallel} - I_{\perp}}{I_{\parallel} + 2I_{\perp}} \tag{13}$$

 I_{\parallel} and I_{\perp} are the parallel and perpendicular intensities of the emitted light, respectively, and r is the fluorescence anisotropy.

The anisotropy of a frozen sample that does not rotate is the fundamental anisotropy r_0 , which depends on the angle ξ between the absorption and emission transition dipole moments as described by 120

$$r_0 = \frac{3\cos^2 \xi - 1}{5} \tag{14}$$

For a sample in solution, rotation of excited-state fluorophores leads to emission-dipole spatial displacement relative to the corresponding frozen sample, resulting in depolarization of the emitted light and a fluorescence anisotropy value smaller than r_0 . The degree of depolarization depends on the extent of rotational diffusion of the fluorophores during their fluorescent lifetime. Therefore, anisotropy measurements can be used to measure the rotational diffusion of the sample, which can provide information about the shape, size, and dynamics of the molecule. Importantly, fluorescence anisotropy can only sense dynamics that occur on timescales similar or faster than the lifetime of the fluorophore, which typically range from 0.1 to 20 ns. 121 While steady-state anisotropy reports on the average anisotropy for all rotational motions, anisotropy decay measurements can resolve the timescales and amplitudes of different motions experienced by the fluorophore (Figure 5). In this work, we measure fluorescence anisotropy decay in the frequency domain to resolve the rotational motion of the compact portion of the nascent chain from the motions of the ribosome and fluorescent probe (see the Supporting



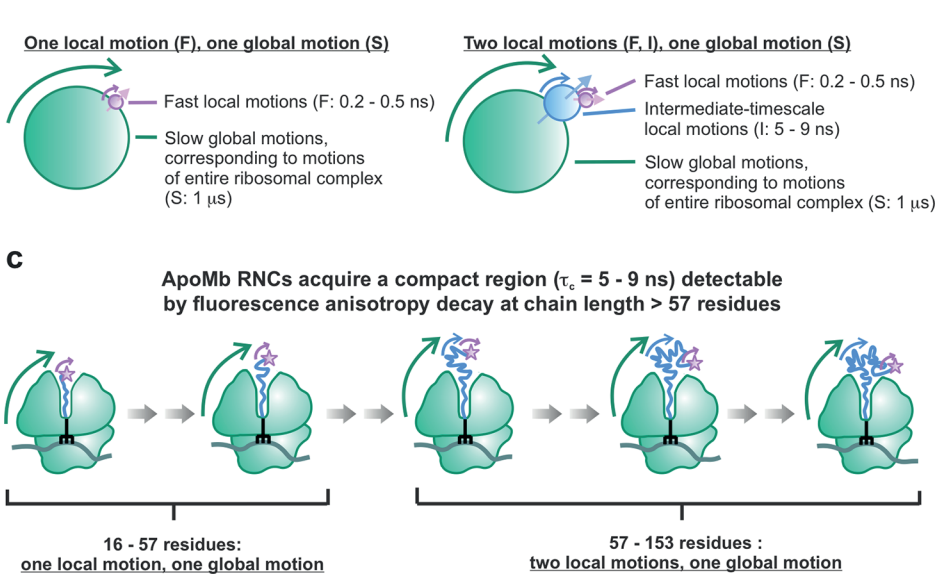


Figure 5. Fluorescence anisotropy decays measured in the frequency domain enable resolving multiple rotational modes, including one corresponding to an apoMb RNC compact subdomain (rotational correlation time $\tau_c = 5-9$ ns). (a) Simulations of two- and three-component frequency-domain anisotropy decay data. (b) Representative physical models for samples with one global tumbling motion one or two local tumbling motions. (c) Prior anisotropy decay data revealed that apoMb nascent chains become compact and tumble independently starting from chain lengths of ca. 57 residues.¹³

Information and supporting Figure S2 for further discussion on steady-state versus time-decay and time-domain *versus* frequency-domain approaches).

Order Parameters and Cone Semiangles Define the Spatial Confinement of Rotational Motions. In addition to sensing the compaction of nascent chains, fluorescence anisotropy-decay measurements also provide information on the spatial confinement of nascent-chain dynamics. The Lipari-Szabo approach provides a model-free method to determine an order parameter that describes the spatial confinement of a rotational motion based on that motion's fractional contribution to the anisotropy decay. 58,122 Order parameters range from 0 to 1, where higher-order parameters describe more highly constrained motions. The Lipari-Szabo method does not require a specific model to describe the motions, but it does depend on the following five assumptions: (i) the fluorophore has axial symmetry. (ii) Either the fluorescence absorption or emission dipole is colinear with the fluorophore's symmetry axis. (iii) The local fast motions are random and do not depend on the azimuthal angle ϕ

(Figure 6). (iv) The local and global motions are independent of each other. (v) The rotational correlation times of the motions differ by an order of magnitude or more. For a system that meets these requirements, the anisotropy decay is described by eqs 15 and 16 in the case of two and three rotational motions, respectively.

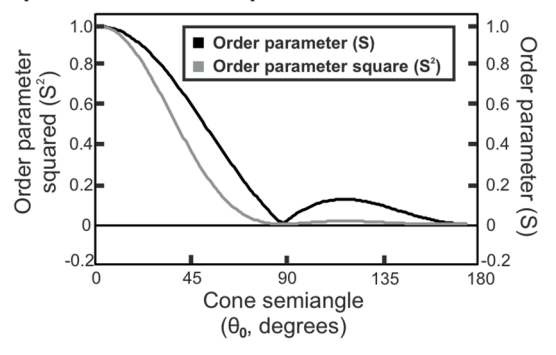
$$\frac{r(t)}{r(0)} = (1 - S_F^2)e^{-t/\tau_{c,F}} + (S_F^2)e^{-t/\tau_{c,S}}$$
(15)

$$\frac{r(t)}{r(0)} \cong (1 - S_F^2) e^{-t/\tau_{c,F}} + (S_F^2) (1 - S_I^2) e^{-t/\tau_{c,I}} + S_F^2 S_I^2$$

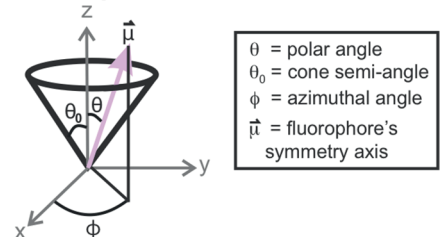
$$e^{-t/\tau_{c,S}} \tag{16}$$

Specific models can be used to gain a more intuitive appreciation for the nature of the spatial confinement encoded by the order parameter. We employed a model by Kinosita et al. that assumes local motions to be confined across a cone according to a square-well potential. ¹²³ In this way, we were able to determine limiting cone semiangles from order

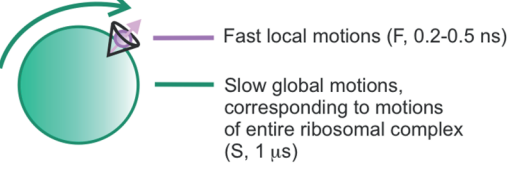
a Dependence of order parameter on cone semi-angle



b Cone semi-angles define the maximum amplitude of local motions



c Local and global dynamics of ribosome-bound nascent chains (RNCs) One local motion (F), one global motion (S)



Two local motions (F, I), one global motion (S)

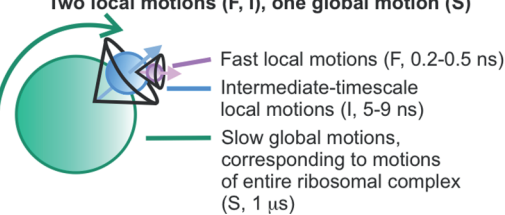


Figure 6. Order parameters and cone semiangles define the spatial confinement of nascent-chain dynamics. (a) Dependence of order parameter on the cone semiangle, assuming a square-well potential. (b) General features of cone semiangle models. The vector $\overrightarrow{\mu}$ defines the fluorophore's symmetry axis, whose orientation can fluctuate so that its angle with the z-axis (θ) is less than or equal to the cone semiangle θ_0 . The motions are randomly distributed within the XY plane and can assume any value of the azimuthal angle ϕ . The z-axis is defined to be perpendicular to the macromolecular surface the tumbling species is attached to. (c) Cartoon description of macromolecules bearing either one or two local motions that are spatially confined within a cone.

parameters, thus gaining a more physically meaningful description, as shown in Figure 6. 123 The position of the symmetry axis of the rotating species $(\vec{\mu})$ can be described by 123

$$p_{\text{eq}}(\theta) = [2\pi(1 - \cos\theta_0)]^{-1} \text{ for } 0 \le \theta \le \theta_0$$
 (17)

$$p_{\rm eq}(\theta) = 0 \text{ for } \theta > \theta_0 \tag{18}$$

where $p_{\rm eq}(\theta)$ is the normalized equilibrium distribution of the angle θ and θ_0 is the limiting cone semiangle. Within this model, the order parameter can be converted to the cone semiangle according to

$$S_i^2 = \left[\frac{1}{2}\cos\theta_0(1-\cos\theta_0)\right]^2$$
 (19)

The abovementioned equations are powerful because they enable assessing the spatial confinement of rotational motions.

Biologically Significant Application: Identification of Size and Dynamics of a Ribosome-Bound Nascent Chain. Full-length apoMb ribosome-nascent protein complexes displayed three rotational motions, consistent with previous results. ¹³ Figure 7 shows representative fluorescence

Representative fluorescence anisotropy decay data

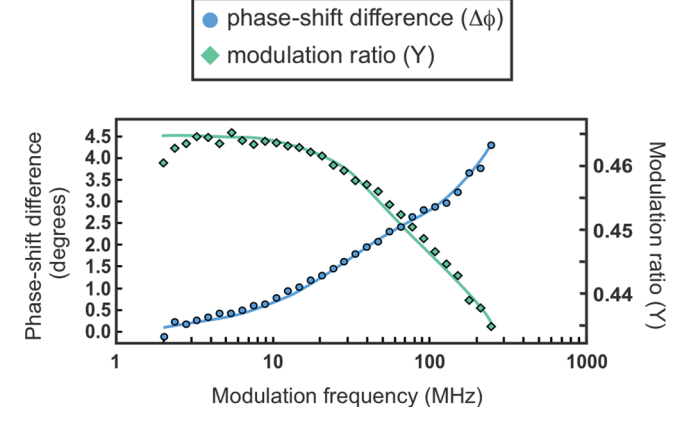


Figure 7. Representative frequency-domain fluorescence anisotropy-decay data for full-length apoMb RNCs.

anisotropy decays in the frequency domain. Lifetime and anisotropy decay data for all samples are shown in supporting Figure S3. The rotational correlation times corresponding to these motions are summarized in Table 1. The rotational correlation time for the global tumbling of the ribosomal complex was fixed to 1000 ns. This global rotational correlation time cannot be detected directly because it occurs on a significantly longer timescale than the lifetime of BODIPY-FL (5.9 ns). On the other hand, its presence (in the context of spatially biased faster local motions) is evident from the fact that the anisotropy does not completely decay to zero. The fast motions ($\tau_c = 0.14 \pm 0.01$ ns) have a rotational correlation time corresponding to free BODIPY-FL linked to 1-2 residues; hence, these motions describe the dynamics of the RNC N-terminus. 15 The intermediate timescale motions $(\tau_c = 3.7 \pm 0.5 \text{ ns})$ correspond to the motions of a compact region of the nascent chain that tumbles independently from the ribosome. These results agree with previous anisotropydecay investigations.¹³

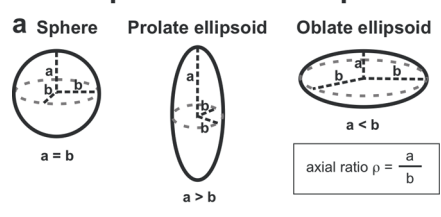
In order to determine the size of the compact domain, apoMb nascent chains were modeled as either spheres, prolate ellipsoids, or oblate ellipsoids (Figure 8). Full-length apoMb nascent chains are unlikely to exist as an extended chain because the persistence length of proteins is typically only 4–6 amino acids.¹³ The experimentally measured solution viscosity and rotational correlation times were used to determine the

Table 1. Summary of Rotational Correlation Times and Number of Amino Acids in Compact Nascent-Chain Domains

regime	s of motion ^a							
slow (~microsecond or slower)	intermediate (~ns)	fast (~ps)	number of amino acids in compact domain			percent of chain in compact domain		
$ au_{\mathrm{c,S}}$ (ns)	$ au_{\mathrm{c,I}}$ (ns)	$ au_{\mathrm{c,F}}$ (ns)	sphere	prolate ellipsoid $(\rho = 3.5)$	oblate ellipsoid $(\rho = 0.5)$	sphere	prolate ellipsoid	oblate ellipsoid
1000	3.7 ± 0.5	0.14 ± 0.01	83 ± 10	57 ± 7	68 ± 9	$54\pm7\%$	$37\pm5\%$	$45\pm6\%$

^aData are reported as average \pm SE for n = 9.

Representative compact-domain shapes



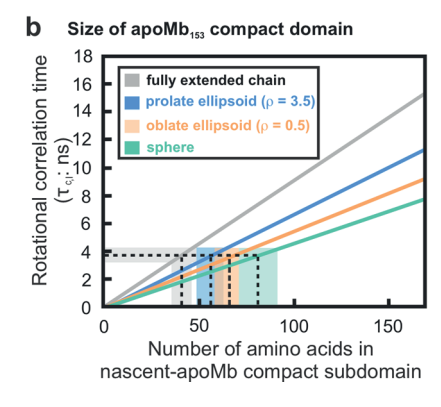


Figure 8. Size of the RNC compact subdomain can be deduced from the experimental rotational correlation time (for the low-nanosecond motion) and from the experimentally determined viscosity. Three limiting molecular shapes were considered: (a) spherical, prolate ellipsoid (axial ratio = 3.5), and oblate ellipsoid (axial ratio = 0.5). (b) Plot illustrating the experimentally determined rotational correlation time for the intermediate timescale motions ($\tau_{\rm c,l}$) as a function of number of amino acids in the compact subdomain. Domain sizes compatible with experimentally determined rotational correlation times are shaded in color (blue, orange, and green).

number of amino acids contained in the compact region of the nascent chain. The SED relation (eq 12) was used to determine the size of the compact domain assuming a spherical shape. The nascent chain was also modeled as a prolate ellipsoid (representative axial ratio of 3.5) and an oblate ellipsoid (representative axial ratio 0.5). The equations used for these models are included in Figure 2 and in the Supporting Information.

Our results show that the RNC compact region comprises 57 to 83 amino acids (37–54% of the nascent chain, see Table 1). Therefore, we are able to eliminate Figure 1's model d, which entails a small-size compact subdomain (Figure 9). It is worth noting that our data are insensitive to other potential extended or compact RNC conformations interacting with the ribosome or molecular chaperones.

Spatial Confinement of Nascent-Chain Motions. In addition to determining the size of the compact domain, we also determined the spatial confinement of the nascent-chain dynamics (see Table 2). The cone semiangles for the fast and intermediate motions are $24.3 \pm 0.8^{\circ}$ and $15.3 \pm 0.7^{\circ}$,

Limiting models for ribosome-bound nascent chain (RNC) compaction and size

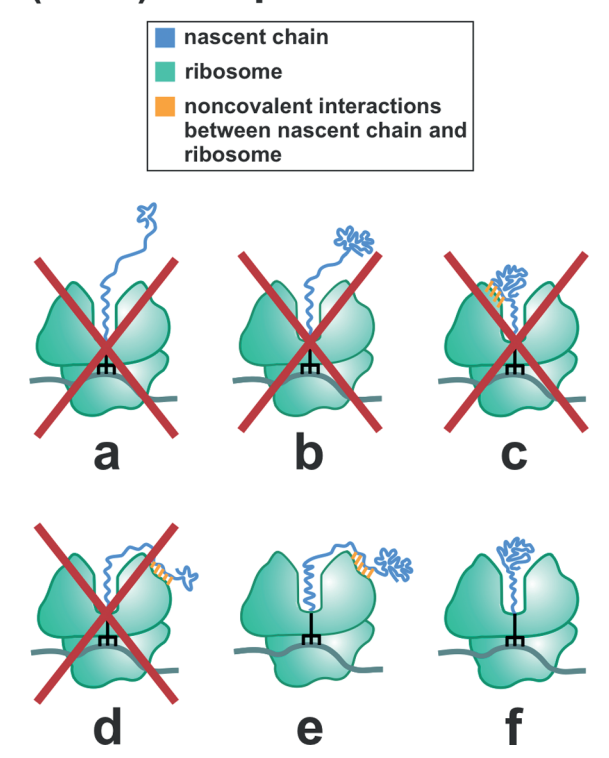


Figure 9. RNC models compatible with experimentally determined rotational correlation times and viscosity values.

Table 2. Summary of Order Parameters and Cone Semiangles for apoMb-RNC Rotational Motions

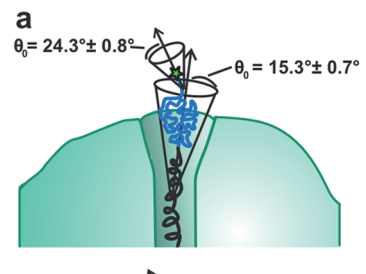
regimes of motion ^a								
intermediat	e (~ns)	fast (~ps)						
S_{I}	θ_0 (deg)	$S_{ m F}$	θ_0 (deg)					
0.947 ± 0.005	15.3 ± 0.7	0.87 ± 0.01	24.3 ± 0.8					

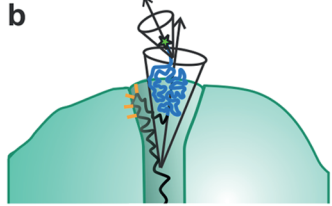
^aData are reported as average \pm SE for n = 9.

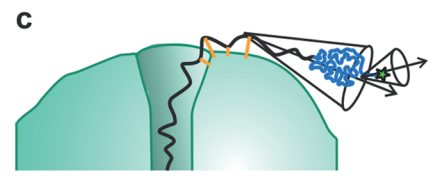
respectively.¹⁵ These cone semiangles are quite small as the maximum size for a cone semiangle is 180°, indicating that the amplitude of the compact RNC-domain motions is spatially constrained.¹⁵ The small cone semiangles suggest that the compact subdomain may be confined within the ribosomal vestibule or near the ribosome surface (Figure 10). Previous work showed that the ribosomal vestibule is sufficiently large to accommodate the nascent protein tertiary structure^{10,12} and even proteins as large as 108 amino acids.⁴³ Therefore, the vestibule accommodates the apoMb compact structure which

Cone semi-angles show the highly geometrically constrained environment of nascent chains

independently-tumbling compact region
 remaining residues
 noncovalent interactions between the nascent chain and the ribosome







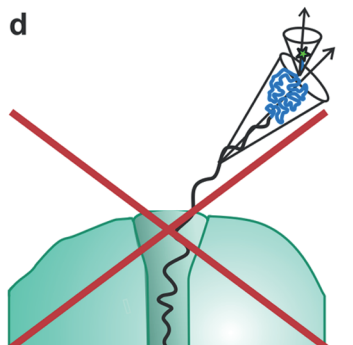


Figure 10. RNC models compatible with spatially confined dynamics described by experimental cone semiangles. The spatial confinement of the nascent-chain dynamics suggests that the compact domain lies within the ribosomal vestibule or is somehow spatially confined within the outer surface of the ribosome.

contains 57–83 amino acids. Alternatively, a portion of the chain prior to compact region may interact with the outer ribosomal surface, causing the compact subdomain to be outside of the ribosomal tunnel altogether.

Potential Interactions of Nascent Chains and Ribosome (or Chaperones) Do not Affect the Estimated Size of the Compact Region of the Nascent Chain. Until now, this work disregarded any potential interactions between nascent chains and the ribosomal surface or molecular chaperones. In principle, these interactions may affect the size of the compact region. Here, we show that the presence of any interactions does not affect the estimated size of the compact region.

Recent studies show that some nascent chains include populations experiencing noncovalent contacts with the ribosome ^{26,124,125} and/or chaperones. ^{13,126–129} A study by Ellis et al. ¹³ showed that the observed rotational correlation time of apoMb RNCs is the same in the absence and presence of trigger factor and DnaK. This work showed that although chaperone-bound RNC populations are likely present, their effect on fluorescence anisotropy decays is spectroscopically undetectable. ¹³ The arguments below show that a similar conclusion applies to nascent-chain interactions with the ribosomal surface.

First, even the most rapid (i.e., diffusion-controlled) conformational exchange of RNCs with the ribosomal surface is too slow to be fully averaged during the fluorescence anisotropy decay timescale (see derivation in the Supporting Information). Thus, any interacting populations are in slow exchange on the fluorescence timescale of our measurements and therefore correspond to distinct nonaveraged contributions. Second, the effect of ribosome-interacting and non-interacting populations on the observed anisotropy-decay parameters was explicitly evaluated and shown not to affect observed rotational correction times corresponding to low-nanosecond intermediate timescale RNC motions.

Briefly, let us denote independently tumbling compact RNC populations as contributing (C) and populations interacting with the ribosomal surface as noncontributing (NC). NC RNCs show two rotational correlation times (fast and slow) and contributing RNCs show a third intermediate timescale (ns) rotational correlation time corresponding to the independently tumbling nascent protein. A mixture including both populations has an anisotropy decay described by the relation below¹⁵

$$\frac{r_{\text{obs}}(t)}{r_0} = [x_{\text{C}}(1 - S_{\text{F,C}}^2) + x_{\text{NC}}(1 - S_{\text{F,C}}^2)]e^{(-t/\tau_{c,\text{F}})}
+ x_{\text{C}}S_{\text{F,C}}^2(1 - S_{\text{I,C}}^2)e^{(-t/\tau_{c,\text{I}})}
+ (x_{\text{C}}S_{\text{I,C}}^2S_{\text{F,C}}^2 + x_{\text{NC}}S_{\text{F,NC}}^2)e^{(-t/\tau_{c,\text{S}})}$$
(20)

where $x_{\rm C}$ and $x_{\rm NC}$ are the mole fractions of the contributing and noncontributing species, respectively. Equation 20 is explicitly derived in the Supporting Information. Importantly, this relation follows a three-component exponential decay that displays the same rotational correlation times as those of RNCs that do not interact with the ribosome.

In summary, eq 20 shows that the presence of RNCs interacting with the ribosome does not affect the experimental rotational correlation times and the estimated size of the compact domain experiencing the low-nanosecond intermediate timescale motions.

Next, we asked whether the presence of ribosome (or chaperone) nascent-chain interactions may affect the observed amplitude of RNC nanosecond motions. On the other hand, eq 20 also shows that the presence of any ribosome-interacting population is expected to affect the observed order parameter and cone semiangle corresponding to the intermediate timescale motion. Hence these parameters are numerically different in the absence and presence of interactions with the ribosomal surface, as shown in Table S4. Interestingly, Table S4 shows that even if the contributing (i.e., noninteracting) species has a mole fraction of only 0.2, the cone semiangle for the intermediate timescale motions is at most 39°, which is significantly less than the maximum value of 180°. This small

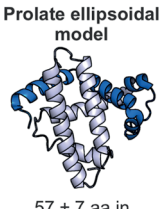
cone semiangle value confirms that regardless of any ribosome (or chaperone) interactions with the nascent protein, the nascent-chain motions are highly spatially confined.

Compact Region of Full-Length apoMb RNCs Lacks Residues Corresponding to the Two Native C-Terminal Helices. The combined anisotropy/microscale-volume viscometry approach reveals that the compact subdomain of full-length apoMb RNCs lacks residues corresponding to the two native C-terminal helices, denoted as the G and H helices (Figure 11). While previous work demonstrated that the C-

Native C-terminal helices are not available for folding into the native state until after ribosome-release

a Independently-tumbling-compact domain of apoMb₁₅₃ RNCs mapped onto native structure

 independently-tumbling-compact domain (mapped onto native structure)
 remaining residues (mapped onto native structure)





57 ± 7 aa in compact domain

83 ± 10 aa in compact domain

b RNC structures compatible with fluorescence anisotropy and viscosity data

independently-tumbling-compact domain
 remaining residues
 noncovalent interactions between
 the nascent chain and the ribosome

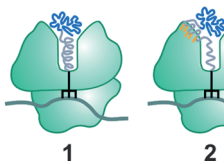




Figure 11. Compact nascent-apoMb subdomain does not include residues corresponding to the native C-terminal helices. (a) Size of the independently tumbling compact subdomain mapped onto the structure of native apoMb. (b) RNC structures compatible with our experimental data.

terminal H helix plays an important role in enabling apoMb to fold into its native state, this study provides the first experimental evidence that the major RNC compact domain does not contain the residues corresponding to the G helix.

Most single-domain proteins require the C-terminal region in order to fold into their native state. The C-terminal region is important for folding because it buries nonpolar residues. ¹³⁰ Fragments of these proteins without the C-terminal region have more nonpolar solvent-accessible surface area than the full-length native structure, making them more likely to misfold and aggregate. ¹³⁰ The C-terminal region is also important for folding because the native structures of many single-domain proteins have interactions between the protein N- and C-terminal regions. ^{131,132} These long-range interactions with the C-terminal region make post-translational folding important for the protein to reach its final native structure. ^{30,133}

The experimental finding that the residues corresponding to the G helix are not contained in the compact region can be rationalized with the help of NECNOP plots. These plots predict whether proteins are capable of being folded or disordered at ambient temperature and pressure based solely on net-charge and nonpolar content. NECNOP plots contain a discriminant line that separates folded proteins (right side of the line) from unfolded proteins or intrinsically disordered proteins (left side of line). The discriminant line is defined as 134

$$|MNC| = 12.0698 \times MNPC - 8.4815$$
 (21)

where lMNCl is the absolute value of mean net charge per residue and MNPC is the mean nonpolar content per residue.

Importantly, the NECNOP plot demonstrates that the G helix adds nonpolar residues to the chain, increasing the overall hydrophobicity of the protein. However, our work demonstrates that the full-length ribosome-bound apoMb does not bury the G-helix residues in a compact structure. Additionally, the predicted folding free energy of apoMb fragments containing the residues corresponding to the G helix but excluding the residues corresponding to the H helix is unfavorable (Figure 12d, predicted folding free energy calculated with FoldX version 5¹³⁵). Folding into the native state without the H helix present is likely unfavorable because the G-helix residues do not play a significant role in burying nonpolar residues, as shown by Kurt and Cavagnero and Figure 12c. 130 Given that residues corresponding to the native G helix are not included in the compact subdomain of ribosome-bound apoMb, they must bury their nonpolar content in another way, perhaps by interacting with the ribosome or by forming some structure (potentially helical)¹³ compatible with the ribosomal tunnel core (Figure 11b).

The NECNOP plot also shows that the H-helix residues decrease the overall hydrophobicity of the protein. Therefore, the residues belonging to the H helix are not particularly nonpolar, but they are very effective at burying nonpolar residues (Figure 12c). 130 Additionally, the H helix has a higher residue-specific contact order (RCO) and residue contact breadth (RCB) compared to the middle region of the protein. 131 RCO is a measure of the number of long-range interactions, such as interactions between the C-terminal residues and the N-terminal residues, within a given region of a protein. RCB is a measure of the spread in sequence of the interactions. 131 Therefore, the relatively high RCO and RCB of the H-helix residues demonstrate that this region interacts with regions spanning a large sequence range of the protein, including the N-terminal residues. Therefore, the H-helix residues form an integral part of the native structure. The breadth of interactions that the H-helix residues have with the rest of the protein and their ability to bury nonpolar residues contribute to the favorable folding energy when the H helix is present (Figure 12d).

Implications for Cotranslational Conformation of Full-Length apoMb RNCs. Our results demonstrate that the residues corresponding to the G helix of full-length ribosome-bound apoMb do not belong to the compact subdomain. Therefore, this region must bury its nonpolar residues through other interactions, which suggests that these residues either interact with the ribosomal vestibule or surface, or are involved in the tight secondary structure within spatially constrained core regions of the ribosomal tunnel (Figure 11b). Additionally, because the compact subdomain does not contain the H helix that plays an important role in burying nonpolar residues, this compact region may be a non-native

Computational data explain why G-helix residues are not contained in the compact subdomain

a Native-state structure of apoMb



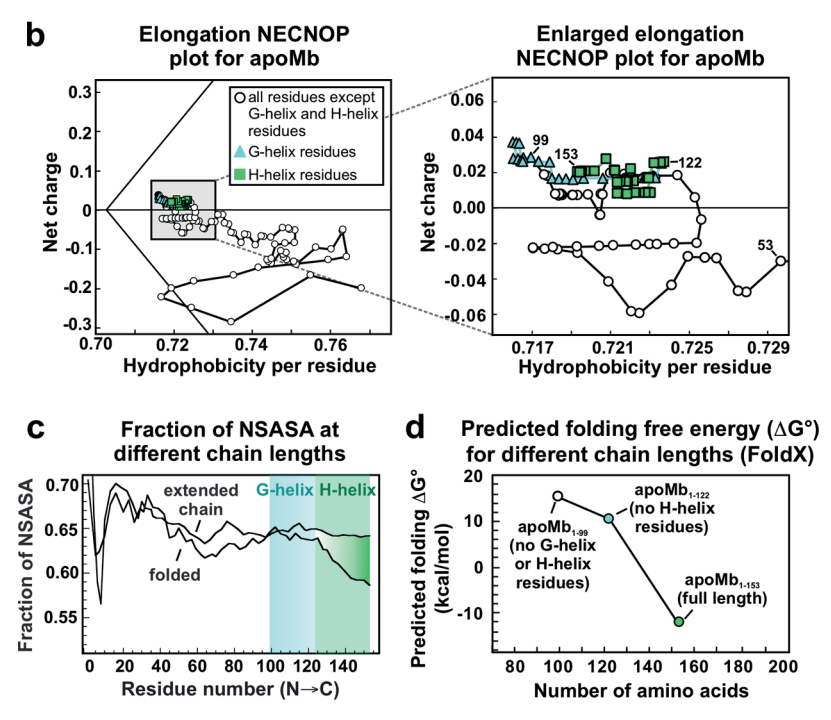


Figure 12. Computational data rationalizing why the nascent-apoMb compact subdomain lacks residues corresponding to the native G helix. (a) Native apoMb structure with G and H helices colored in blue and green, respectively. (b) Elongation net-charge nonpolar (NECNOP) plot for apoMb generated according to Yaeger-Weiss et al. ¹³⁴ The black discriminant line separates regions corresponding to folded (right of line) and disordered proteins (left of line). (c) Fraction of the nonpolar solvent-accessible surface area (NSASA) at different apoMb chain lengths. Adapted with permission from Kurt, N.; Cavagnero, S. J. Am. Chem. Soc. 2005, 127 (45), 15690–15691. ¹³⁰ Copyright (2005) American Chemical Society. (d) Predicted free energy of folding for different apoMb chain lengths. See supporting Figure S6 for predicted folding free energies of additional chain lengths. All free-energy calculations were carried out with FoldX version 5. ¹³⁵ PDB files for apoMb (RCSB PDB: 1mbc) were generated with Pymol version 2.0.0.

conformation that buries the N-terminal nonpolar residues until the H helix is available for folding. The compaction of nascent chain and the interaction of the residues corresponding to the G helix with the ribosome may help to keep the nascent chain soluble and prevent it from misfolding until the H-helix residues are available for folding into the native structure.

Implications for Post-translational Folding. Previous work demonstrated that cotranslational folding is not sufficient for apoMb to fold into its native structure but rather that immediately post-translational events are vital for folding.³⁰ Immediately post-translational folding is a critical and potentially dangerous time during which nascent chains must be kinetically channeled to their native state or they risk forming an aggregated state.³⁰ Our findings explain why this post-translational period is so critical because they quantify the amount of required post-translational folding, revealing that apoMb must incorporate more than 60 amino acids into the final structure post-translationally, not just the final 30–40 residues contained within the ribosomal exit tunnel. These results demonstrate that while apoMb undergoes cotransla-

tional compaction, this protein still requires significant posttranslational folding to obtain its final native structure.

CONCLUSIONS

In summary, our results demonstrate that only a portion (57– 83 amino acids, 37-54% of the chain) of the full-length apoMb RNC forms a compact core. Specifically, residues belonging to the native G and H helices do not belong to this compact domain. In all, our results demonstrate that the model single-domain protein apoMb must undergo considerable additional folding after ribosome release. Therefore, our data suggest that the immediately post-translational folding of single-domain proteins is a prominent theme whose importance has been underestimated to date. Furthermore, our findings underscore the importance of a proper supporting machinery (e.g., molecular chaperones) to prevent protein aggregation upon nascent-protein release from the ribosome. The spatial confinement of the nascent-protein local dynamics suggests that the compact subdomain is located within the ribosomal vestibule or within spatially biased regions of the outer surface of the ribosome.

Furthermore, our results demonstrate that microscale-volume viscometry combined with fluorescence anisotropy decay is a powerful approach to investigate the compaction and dynamics of RNCs. The technology presented in this work is simple, versatile, and of general applicability. Conveniently, this method only requires a single fluorophore and no C-terminal linkers.

ASSOCIATED CONTENT

Supporting Information

The Supporting Information is available free of charge at https://pubs.acs.org/doi/10.1021/acs.jpcb.1c04473.

Puromycin-assay description and representative SDS-PAGE gels, comparisons between steady-state anisotropy and time-domain and frequency-domain anisotropy decays, determination of reduced χ^2 values, potential effect of ribosome—nascent-chain interactions on anisotropy parameters, oligonucleotide sequences used in cell-free reactions, anisotropy-decay graphs for all the data collected in this work, and predicted standard-state folding free energies for several nascent-chain lengths (PDF)

AUTHOR INFORMATION

Corresponding Author

Silvia Cavagnero — Department of Chemistry, University of Wisconsin-Madison, Madison, Wisconsin 53706, United States; orcid.org/0000-0002-4290-2331; Email: cavagnero@chem.wisc.edu

Authors

Rachel B. Hutchinson – Department of Chemistry, University of Wisconsin-Madison, Madison, Wisconsin 53706, United States; orcid.org/0000-0002-9645-2970

Xi Chen – Department of Chemistry, University of Wisconsin-Madison, Madison, Wisconsin 53706, United States;
ocid.org/0000-0002-8458-3594

Ningkun Zhou — Department of Chemistry, University of Wisconsin-Madison, Madison, Wisconsin 53706, United States; orcid.org/0000-0001-7596-1568

Complete contact information is available at: https://pubs.acs.org/10.1021/acs.jpcb.1c04473

Notes

The authors declare no competing financial interest.

ACKNOWLEDGMENTS

We thank the National Science Foundation (NSF) for funding (grants MCB-1616459 and CBET 1912259 to S.C.). In addition, R.H. thanks the National Institute of General Medical Sciences of the National Institutes of Health for a TEAM-Science Fellowship (award number R25GM083252). The content of this publication is solely the responsibility of the authors and does not necessarily represent the official views of the National Institutes of Health. We are thankful for a grant from the Graduate School and the Office of the Vice Chancellor for Research and Graduate Education at the University of Wisconsin—Madison (to S.C.). We are grateful to Valeria Guzman-Luna for help with the generation of supporting Figure S5. Finally, we thank Grace Baek and Gordon Stack (Rheosense), Javier Delgado Blanco (FoldX expert), Shih-Chu Liao (ISS), and all members of the

Cavagnero group for technical assistance and helpful discussions.

REFERENCES

- (1) Dill, K. A.; MacCallum, J. L. The protein-folding problem, 50 years on. *Science* **2012**, 338, 1042–1046.
- (2) Sosnick, T. R.; Barrick, D. The folding of single domain proteins—have we reached a consensus? *Curr. Opin. Struct. Biol.* **2011**, *21*, 12–24.
- (3) Udgaonkar, J. B. Polypeptide chain collapse and protein folding. *Arch. Biochem. Biophys.* **2013**, *531*, 24–33.
- (4) Fedyukina, D. V.; Cavagnero, S. Protein folding at the exit tunnel. *Annu. Rev. Biophys.* **2011**, *40*, 337–359.
- (5) Balchin, D.; Hayer-Hartl, M.; Hartl, F. U. In vivo aspects of protein folding and quality control. *Science* **2016**, 353, aac4354.
- (6) Braselmann, E.; Chaney, J. L.; Clark, P. L. Folding the proteome. Trends Biochem. Sci. **2013**, 38, 337–344.
- (7) Gruebele, M.; Dave, K.; Sukenik, S. Globular protein folding in vitro and in vivo. *Annu. Rev. Biophys.* **2016**, *45*, 233–251.
- (8) Waudby, C. A.; Dobson, C. M.; Christodoulou, J. Nature and regulation of protein folding on the ribosome. *Trends Biochem. Sci.* **2019**, *44*, 914–926.
- (9) Lu, J.; Deutsch, C. Folding zones inside the ribosomal exit tunnel. *Nat. Struct. Mol. Biol.* **2005**, *12*, 1123–1129.
- (10) Kosolapov, A.; Deutsch, C. Tertiary interactions within the ribosomal exit tunnel. *Nat. Struct. Mol. Biol.* **2009**, *16*, 405–411.
- (11) Tu, L. W.; Deutsch, C. A folding zone in the ribosomal exit tunnel for Kv1.3 helix formation. J. Mol. Biol. 2010, 396, 1346–1360.
- (12) Tu, L.; Khanna, P.; Deutsch, C. Transmembrane segments form tertiary hairpins in the folding vestibule of the ribosome. *J. Mol. Biol.* **2014**, 426, 185–198.
- (13) Ellis, J. P.; Bakke, C. K.; Kirchdoerfer, R. N.; Jungbauer, L. M.; Cavagnero, S. Chain dynamics of nascent polypeptides emerging from the ribosome. *ACS Chem. Biol.* **2008**, *3*, 555–566.
- (14) Hardesty, B.; Kramer, G. Folding of a nascent peptide on the ribosome. *Prog. Nucleic Acid Res. Mol. Biol.* **2001**, *66*, 41–66.
- (15) Ellis, J. P.; Culviner, P. H.; Cavagnero, S. Confined dynamics of a ribosome-bound nascent globin: Cone angle analysis of fluorescence depolarization decays in the presence of two local motions. *Protein Sci.* **2009**, *18*, 2003–2015.
- (16) Kudlicki, W.; Coffman, A.; Kramer, G.; Hardesty, B. Ribosomes and ribosomal RNA as chaperones for folding of proteins. *Folding Des.* **1997**, *2*, 101–108.
- (17) Chattopadhyay, S.; Das, B.; Dasgupta, C. Reactivation of denatured proteins by 23S ribosomal RNA: Role of domain V. *Proc. Natl. Acad. Sci. U.S.A.* **1996**, 93, 8284–8287.
- (18) Das, B.; Chattopadhyay, S.; Gupta, C. D. Reactivation of denatured fungal glucose 6-phosphate dehydrogenase and E. coli alkaline phosphatase with E. coli ribosome. *Biochem. Biophys. Res. Commun.* 1992, 183, 774–780.
- (19) Samanta, D.; Das, A.; Bhattacharya, A.; Basu, A.; Das, D.; DasGupta, C. Mechanism of ribosome assisted protein folding: A new insight into rRNA functions. *Biochem. Biophys. Res. Commun.* **2009**, 384, 137–140.
- (20) Das, D.; Samanta, D.; Hasan, S.; Das, A.; Bhattacharya, A.; Dasgupta, S.; Chakrabarti, A.; Ghorai, P.; Das Gupta, C. Identical RNA-protein interactions in vivo and in vitro and a scheme of folding the newly synthesized proteins by ribosomes. *J. Biol. Chem.* **2012**, 287, 37508–37521.
- (21) Pang, Y.; Kovachev, P.; Sanyal, S. Ribosomal RNA modulates aggregation of the podospora prion protein HET-s. *Int. J. Mol. Sci.* **2020**, *21*, 6340.
- (22) Ziv, G.; Haran, G.; Thirumalai, D. Ribosome exit tunnel can entropically stabilize α -helices. *Proc. Natl. Acad. Sci. U.S.A.* **2005**, *102*, 18956–18961.
- (23) Woolhead, C. A.; McCormick, P. J.; Johnson, A. E. Nascent membrane and secretory proteins differ in FRET-detected folding far inside the ribosome and in their exposure to ribosomal proteins. *Cell* **2004**, *116*, 725–736.

- (24) Cruz-Vera, L. R.; Rajagopal, S.; Squires, C.; Yanofsky, C. Features of ribosome-peptidyl-tRNA interactions essential for tryptophan induction of tna operon expression. *Mol. Cell* **2005**, *19*, 333–343.
- (25) Houben, E. N. G.; Zarivach, R.; Oudega, B.; Luirink, J. Early encounters of a nascent membrane protein: specificity and timing of contacts inside and outside the ribosome. *J. Cell Biol.* **2005**, *170*, 27–35.
- (26) Guzman-Luna, V.; Fuchs, A. M.; Cavagnero, S. Interaction of an intrinsically disordered nascent protein with specific regions of the ribosomal surface. **2021**, Under revision.
- (27) Ullers, R. S.; Houben, E. N. G.; Raine, A.; ten Hagen-Jongman, C. M.; Ehrenberg, M.; Brunner, J.; Oudega, B.; Harms, N.; Luirink, J. Interplay of signal recognition particle and trigger factor at L23 near the nascent chain exit site on the Escherichia coli ribosome. *J. Cell Biol.* 2003, 161, 679–684.
- (28) Peterson, J. H.; Woolhead, C. A.; Bernstein, H. D. The conformation of a nascent polypeptide inside the ribosome tunnel affects protein targeting and protein folding. *Mol. Microbiol.* **2010**, *78*, 203–217.
- (29) Wang, S.; Jomaa, A.; Jaskolowski, M.; Yang, C.-I.; Ban, N.; Shan, S.-o. The molecular mechanism of cotranslational membrane protein recognition and targeting by SecA. *Nat. Struct. Mol. Biol.* **2019**, 26, 919–929.
- (30) Addabbo, R. M.; Dalphin, M. D.; Mecha, M. F.; Liu, Y.; Staikos, A.; Guzman-Luna, V.; Cavagnero, S. Complementary role of co- and post-translational events in de novo protein biogenesis. *J. Phys. Chem. B* **2020**, *124*, 6488–6507.
- (31) Dao Duc, K.; Batra, S. S.; Bhattacharya, N.; Cate, J. H. D.; Song, Y. S. Differences in the path to exit the ribosome across the three domains of life. *Nucleic Acids Res.* **2019**, *47*, 4198–4210.
- (32) Noeske, J.; Wasserman, M. R.; Terry, D. S.; Altman, R. B.; Blanchard, S. C.; Cate, J. H. D. High-resolution structure of the Escherichia coli ribosome. *Nat. Struct. Mol. Biol.* **2015**, *22*, 336–341.
- (33) Tsalkova, T.; Odom, O. W.; Kramer, G.; Hardesty, B. Different conformations of nascent peptides on ribosomes. *J. Mol. Biol.* **1998**, 278, 713–723.
- (34) Kramer, G.; Ramachandiran, V.; Hardesty, B. Cotranslational folding omnia mea mecum porto? *Int. J. Biochem. Cell Biol.* **2001**, 33, 541–553.
- (35) Malkin, L. I.; Rich, A. Partial resistance of nascent polypeptide chains to proteolytic digestion due to ribosomal shielding. *J. Mol. Biol.* **1967**, *26*, 329–346.
- (36) Nilsson, O. B.; Hedman, R.; Marino, J.; Wickles, S.; Bischoff, L.; Johansson, M.; Müller-Lucks, A.; Trovato, F.; Puglisi, J. D.; O'Brien, E. P.; et al. Cotranslational protein folding inside the ribosome exit tunnel. *Cell Rep.* **2015**, *12*, 1533–1540.
- (37) Marino, J.; von Heijne, G.; Beckmann, R. Small protein domains fold inside the ribosome exit tunnel. *FEBS Lett.* **2016**, 590, 655–660.
- (38) Bhushan, S.; Gartmann, M.; Halic, M.; Armache, J.-P.; Jarasch, A.; Mielke, T.; Berninghausen, O.; Wilson, D. N.; Beckmann, R. α -Helical nascent polypeptide chains visualized within distinct regions of the ribosomal exit tunnel. *Nat. Struct. Mol. Biol.* **2010**, *17*, 313–317.
- (39) Lu, J.; Deutsch, C. Secondary structure formation of a transmembrane segment in Kv channels. *Biochemistry* **2005**, *44*, 8230–8243.
- (40) Liutkute, M.; Maiti, M.; Samatova, E.; Enderlein, J.; Rodnina, M. V. Gradual compaction of the nascent peptide during cotranslational folding on the ribosome. *eLife* **2020**, *9*, No. e60895.
- (41) Farías-Rico, J. A.; Ruud Selin, F.; Myronidi, I.; Frühauf, M.; von Heijne, G. Effects of protein size, thermodynamic stability, and net charge on cotranslational folding on the ribosome. *Proc. Natl. Acad. Sci. U.S.A.* **2018**, *115*, E9280–E9287.
- (42) Tian, P.; Steward, A.; Kudva, R.; Su, T.; Shilling, P. J.; Nickson, A. A.; Hollins, J. J.; Beckmann, R.; von Heijne, G.; Clarke, J.; et al. Folding pathway of an Ig domain is conserved on and off the ribosome. *Proc. Natl. Acad. Sci. U.S.A.* **2018**, *115*, E11284–E11293.

- (43) Nilsson, O. B.; Nickson, A. A.; Hollins, J. J.; Wickles, S.; Steward, A.; Beckmann, R.; von Heijne, G.; Clarke, J. Cotranslational folding of spectrin domains via partially structured states. *Nat. Struct. Mol. Biol.* **2017**, *24*, 221–225.
- (44) Liutkute, M.; Samatova, E.; Rodnina, M. V. Cotranslational folding of proteins on the ribosome. *Biomolecules* **2020**, *10*, 97.
- (45) Bakke, C. K.; Jungbauer, L. M.; Cavagnero, S. In vitro expression and characterization of native apomyoglobin under low molecular crowding conditions. *Protein Expression Purif.* **2006**, *45*, 381–392.
- (46) Gesteland, R. F. Isolation and characterization of ribonuclease I mutants of Escherichia coli. *J. Mol. Biol.* **1966**, *16*, 67–84.
- (47) Springer, B. A.; Sligar, S. G. High-level expression of sperm whale myoglobin in Escherichia coli. *Proc. Natl. Acad. Sci. U.S.A.* **1987**, 84, 8961–8965.
- (48) Behrmann, M.; Koch, H.-G.; Hengelage, T.; Wieseler, B.; Hoffschulte, H. K.; Müller, M. Requirements for the translocation of elongation-arrested, ribosome-associated OmpA across the plasma membrane of Escherichia coli. *J. Biol. Chem.* **1998**, 273, 13898–13904.
- (49) Hanes, J.; Plückthun, A. In vitro selection and evolution of functional proteins by using ribosome display. *Proc. Natl. Acad. Sci. U.S.A.* 1997, 94, 4937–4942.
- (50) Isolation and analysis of ribosomes from prokaryotes, eukaryotes, and organelles. In *Ribosomes and Protein Synthesis: A Practical Approach*; Spedding, G., Ed.; Oxford University Press: Oxford, U.K., 1990; pp 1–27.
- (51) Odom, O. W.; Hardesty, B. Use of 50 S-binding antibiotics to characterize the ribosomal site to which peptidyl-tRNA is bound. *J. Biol. Chem.* **1992**, *267*, 19117–19122.
- (52) Ziehr, D. R.; Ellis, J. P.; Culviner, P. H.; Cavagnero, S. Production of ribosome-released nascent proteins with optimal physical properties. *Anal. Chem.* **2010**, *82*, 4637–4643.
- (53) Moore, S. D.; Baker, T. A.; Sauer, R. T. Forced extraction of targeted components from complex macromolecular assemblies. *Proc. Natl. Acad. Sci. U.S.A.* **2008**, *105*, 11685–11690.
- (54) Schneider, C. A.; Rasband, W. S.; Eliceiri, K. W. NIH image to Image]: 25 years of image analysis. *Nat. Methods* **2012**, *9*, 671–675.
- (5S) Abràmoff, M. D.; Magalhães, P. J.; Ram, S. J. Image processing with ImageJ. *Biophot. Int.* **2004**, *11*, 36–42.
- (56) Beechem, J. M.; Gratton, E. Fluorescence spectroscopy data analysis environment: a second generation global analysis program. In *Time-Resolved Laser Spectroscopy in Biochemistry*; Lakowicz, J. R., Ed.; SPIE: Bellingham, 1988; pp 70–81.
- (57) Ross, J. A.; Jameson, D. M. Time-resolved methods in biophysics. 8. Frequency domain fluorometry: applications to intrinsic protein fluorescence. *Photochem. Photobiol. Sci.* **2008**, *7*, 1301–1312.
- (58) Weinreis, S. A.; Ellis, J. P.; Cavagnero, S. Dynamic fluorescence depolarization: A powerful tool to explore protein folding on the ribosome. *Methods* **2010**, *52*, *57*–*73*.
- (59) Small, E. W.; Isenberg, I. Hydrodynamic properties of a rigid molecule: Rotational and linear diffusion and fluorescence anisotropy. *Biopolymers* **1977**, *16*, 1907–1928.
- (60) Lakowicz, J. R. Principles of Fluorescence Spectroscopy, 3rd ed.; Plenum Press: New York, 2006.
- (61) Kirchdoerfer, R. N.; Huang, J. J.-T.; Isola, M. K.; Cavagnero, S. Fluorescence-based analysis of aminoacyl- and peptidyl-tRNA by low-pH sodium dodecyl sulfate-polyacrylamide gel electrophoresis. *Anal. Biochem.* **2007**, *364*, 92–94.
- (62) Schägger, H.; von Jagow, G. Tricine-sodium dodecyl sulfate-polyacrylamide gel electrophoresis for the separation of proteins in the range from 1 to 100 kDa. *Anal. Biochem.* **1987**, *166*, 368–379.
- (63) Kendrew, J. C.; Bodo, G.; Dintzis, H. M.; Parrish, R. G.; Wyckoff, H.; Phillips, D. C. A three-dimensional model of the myoglobin molecule obtained by x-ray analysis. *Nature* **1958**, *181*, 662–666.
- (64) Kendrew, J. C.; Dickerson, R. E.; Strandberg, B. E.; Hart, R. G.; Davies, D. R.; Phillips, D. C.; Shore, V. C. Structure of myoglobin: a

- three-dimensional fourier synthesis at 2 Å. resolution. *Nature* **1960**, 185, 422–427.
- (65) Jennings, P.; Wright, P. Formation of a molten globule intermediate early in the kinetic folding pathway of apomyoglobin. *Science* **1993**, 262, 892.
- (66) Nishimura, C.; Dyson, H. J.; Wright, P. E. Identification of native and non-native structure in kinetic folding intermediates of apomyoglobin. *J. Mol. Biol.* **2006**, 355, 139–156.
- (67) Eliezer, D.; Wright, P. E. Is apomyoglobin a molten globule? Structural characterization by NMR. J. Mol. Biol. 1996, 263, 531–538.
- (68) Dyson, H. J.; Wright, P. E. How does your protein fold? Elucidating the apomyoglobin folding pathway. *Acc. Chem. Res.* **2017**, *50*, 105–111.
- (69) Armstrong, B. D.; Choi, J.; López, C.; Wesener, D. A.; Hubbell, W.; Cavagnero, S.; Han, S. Site-specific hydration dynamics in the nonpolar core of a molten globule by dynamic nuclear polarization of water. *J. Am. Chem. Soc.* **2011**, *133*, 5987–5995.
- (70) Samatova, E. N.; Melnik, B. S.; Balobanov, V. A.; Katina, N. S.; Dolgikh, D. A.; Semisotnov, G. V.; Finkelstein, A. V.; Bychkova, V. E. Folding intermediate and folding nucleus for $I \rightarrow N$ and $U \rightarrow I \rightarrow N$ transitions in apomyoglobin: contributions by conserved and nonconserved residues. *Biophys. J.* **2010**, *98*, 1694–1702.
- (71) Balobanov, V. A.; Katina, N. S.; Finkelstein, A. V.; Bychkova, V. E. Intermediate states of apomyoglobin: Are they parts of the same area of conformations diagram? *Biochemistry* **2017**, *82*, *625*–*631*.
- (72) Ptitsyn, O. B. Molten globule and protein folding. *Adv. Protein Chem.* **1995**, 47, 83–229.
- (73) Jungbauer, L. M.; Bakke, C. K.; Cavagnero, S. Experimental and computational analysis of translation products in apomyoglobin expression. *J. Mol. Biol.* **2006**, *357*, 1121–1143.
- (74) Jameson, D. M.; Gratton, E.; Hall, R. D. The measurement and analysis of heterogeneous emissions by multifrequency phase and modulation fluorometry. *Appl. Spectrosc. Rev.* **1984**, *20*, 55–106.
- (75) Bucci, E.; Steiner, R. F. Anisotropy decay of fluorescence as an experimental approach to protein dynamics. *Biophys. Chem.* **1988**, *30*, 199–224.
- (76) Feinstein, E.; Deikus, G.; Rusinova, E.; Rachofsky, E. L.; Ross, J. B. A.; Laws, W. R. Constrained analysis of fluorescence anisotropy decay:application to experimental protein dynamics. *Biophys. J.* **2003**, *84*, 599–611.
- (77) Majumdar, A.; Mukhopadhyay, S. Fluorescence depolarization kinetics to study the conformational preference, structural plasticity, binding, and assembly of intrinsically disordered proteins. *Methods Enzymol.* **2018**, *611*, 347–381.
- (78) Shi, X.; Herschlag, D. Fluorescence polarization anisotropy to measure RNA dynamics. *Methods Enzymol.* **2009**, 469, 287–302.
- (79) Liu, C.; Liang, G.; Liu, Z.; Zu, L. Time-resolved fluorescence anisotropy study of the interaction between DNA and a peptide truncated from the p53 protein core domain. *J. Fluoresc.* **2014**, *24*, 533–539.
- (80) Jain, N.; Narang, D.; Bhasne, K.; Dalal, V.; Arya, S.; Bhattacharya, M.; Mukhopadhyay, S. Direct observation of the Iintrinsic backbone torsional mobility of disordered proteins. *Biophys. J.* **2016**, *111*, 768–774.
- (81) Sahay, S.; Anoop, A.; Krishnamoorthy, G.; Maji, S. K. Site-specific fluorescence dynamics of α -synuclein fibrils using time-resolved fluorescence studies: effect of familial Parkinson's disease-associated mutations. *Biochemistry* **2014**, *53*, 807–809.
- (82) Motyka, A. L. An introduction to rheology with an emphasis on application to dispersions. *J. Chem. Educ.* **1996**, *73*, 374–380.
- (83) Jary, D.; Sikorav, J.-L.; Lairez, D. Nonlinear viscoelasticity of entangled DNA molecules. *Europhys. Lett.* **1999**, *46*, 251–255.
- (84) Picchi, D.; Poesio, P.; Ullmann, A.; Brauner, N. Characteristics of stratified flows of Newtonian/non-Newtonian shear-thinning fluids. *Int. J. Multiphase Flow* **2017**, *97*, 109–133.
- (85) Chhabra, R. P. Non-newtonian fluids: an introduction. In *Rheology of Complex Fluids*; Krishnan, J., Deshpande, A., Kumar, P., Eds.; Springer: New York, 2010; pp 3–34.

- (86) Ikeda, S.; Nishinari, K. Solid-like mechanical behaviors of ovalbumin aqueous solutions. *Int. J. Biol. Macromol.* **2001**, 28, 315–320
- (87) Ikeda, S.; Nishinari, K. On solid-like rheological behaviors of globular protein solutions. *Food Hydrocolloids* **2001**, *15*, 401–406.
- (88) Matsumoto, T.; Inoue, H. Colloidal structure and properties of bovine serum globulin aqueous systems using SAXS and rheological measurements. *Chem. Phys.* **1996**, *207*, 167–172.
- (89) Inoue, H.; Matsumoto, T. Viscoelastic characterization of solid-like structure in aqueous colloids of globular proteins. *Colloids Surf., A* **1996**, *109*, 89–96.
- (90) Sharma, V.; Jaishankar, A.; Wang, Y.-C.; McKinley, G. H. Rheology of globular proteins: apparent yield stress, high shear rate viscosity and interfacial viscoelasticity of bovine serum albumin solutions. *Soft Matter* **2011**, *7*, 5150–5160.
- (91) Lu, J. R.; Su, T. J.; Thomas, R. K. Structural conformation of bovine serum albumin layers at the air—water interface studied by neutron reflection. *J. Colloid Interface Sci.* **1999**, 213, 426–437.
- (92) Gouveia, S. M.; Tiffany, J. M. Human tear viscosity: An interactive role for proteins and lipids. *Biochim. Biophys. Acta, Proteins Proteomics* **2005**, 1753, 155–163.
- (93) Allen, S. H.; Wong, K.-P. A comparative study on the hydrodynamic shape, conformation, and stability of E. coli ribosomal subunits in reconstitution buffer. *Arch. Biochem. Biophys.* **1979**, *195*, 112–120.
- (94) Taylor, N.; Elbaum-Garfinkle, S.; Vaidya, N.; Zhang, H.; Stone, H. A.; Brangwynne, C. P. Biophysical characterization of organellebased RNA/protein liquid phases using microfluidics. *Soft Matter* **2016**, *12*, 9142–9150.
- (95) Juarez, G.; Arratia, P. E. Extensional rheology of DNA suspensions in microfluidic devices. *Soft Matter* **2011**, *7*, 9444–9452.
- (96) Ciccolini, L. A. S.; Ayazi Shamlou, P.; Titchener-Hooker, N. J.; Ward, J. M.; Dunnill, P. Rheological properties of chromosomal and plasmid DNA during alkaline lysis reaction. *Bioprocess Eng.* **1999**, 21, 231–237.
- (97) Wang, Y.; Li, C.; Pielak, G. J. Effects of proteins on protein diffusion. J. Am. Chem. Soc. 2010, 132, 9392–9397.
- (98) Mika, J. T.; Poolman, B. Macromolecule diffusion and confinement in prokaryotic cells. *Curr. Opin. Biotechnol.* **2011**, 22, 117–126.
- (99) Dix, J. A.; Verkman, A. S. Crowding effects on diffusion in solutions and cells. *Annu. Rev. Biophys.* **2008**, *37*, 247–263.
- (100) Tabaka, M.; Kalwarczyk, T.; Szymanski, J.; Hou, S.; Holyst, R. The effect of macromolecular crowding on mobility of biomolecules, association kinetics, and gene expression in living cells. *Front. Phys.* **2014**, *2*, 54.
- (101) Theillet, F.-X.; Binolfi, A.; Frembgen-Kesner, T.; Hingorani, K.; Sarkar, M.; Kyne, C.; Li, C.; Crowley, P. B.; Gierasch, L.; Pielak, G. J.; et al. Physicochemical properties of cells and their effects on intrinsically disordered proteins (IDPs). *Chem. Rev.* **2014**, *114*, 6661–6714.
- (102) Li, C.; Wang, Y.; Pielak, G. J. Translational and rotational diffusion of a small globular protein under crowded conditions. *J. Phys. Chem. B* **2009**, *113*, 13390–13392.
- (103) Kuttner, Y. Y.; Kozer, N.; Segal, E.; Schreiber, G.; Haran, G. Separating the contribution of translational and rotational diffusion to protein association. *J. Am. Chem. Soc.* **2005**, *127*, 15138–15144.
- (104) Wiśniewska, A.; Sozański, K.; Kalwarczyk, T.; Kędra-Królik, K.; Pieper, C.; Wieczorek, S. A.; Jakieła, S.; Enderlein, J.; Hołyst, R. Scaling of activation energy for macroscopic flow in poly(ethylene glycol) solutions: Entangled Non-entangled crossover. *Polymer* 2014, 55, 4651–4657.
- (105) Zosel, F.; Soranno, A.; Buholzer, K. J.; Nettels, D.; Schuler, B. Depletion interactions modulate the binding between disordered proteins in crowded environments. *Proc. Natl. Acad. Sci. U.S.A.* **2020**, *117*, 13480–13489.
- (106) Zorrilla, S.; Hink, M. A.; Visser, A. J. W. G.; Lillo, M. P. Translational and rotational motions of proteins in a protein crowded environment. *Biophys. Chem.* **2007**, *125*, 298–305.

- (107) McGuffee, S. R.; Elcock, A. H. Diffusion, crowding & protein stability in a dynamic molecular model of the bacterial cytoplasm. *PLoS Comput. Biol.* **2010**, *6*, No. e1000694.
- (108) Tuinier, R.; Dhont, J. K. G.; Fan, T.-H. How depletion affects sphere motion through solutions containing macromolecules. *Europhys. Lett.* **2006**, *75*, 929–935.
- (109) Asakura, S.; Oosawa, F. Interaction between particles suspended in solutions of macromolecules. *J. Polym. Sci.* 1958, 33, 183–192.
- (110) Vrij, A. Polymers at interfaces and the interactions in colloidal dispersions. *Pure Appl. Chem.* **1976**, *48*, 471–483.
- (111) von Bülow, S.; Siggel, M.; Linke, M.; Hummer, G. Dynamic cluster formation determines viscosity and diffusion in dense protein solutions. *Proc. Natl. Acad. Sci. U.S.A.* **2019**, *116*, 9843–9852.
- (112) Fedyukina, D. V.; Jennaro, T. S.; Cavagnero, S. Charge segregation and low hydrophobicity are key features of ribosomal proteins from different organisms. *J. Biol. Chem.* **2014**, 289, 6740–6750.
- (113) Baker, N. A.; Sept, D.; Joseph, S.; Holst, M. J.; McCammon, J. A. Electrostatics of nanosystems: application to microtubules and the ribosome. *Proc. Natl. Acad. Sci. U.S.A.* **2001**, *98*, 10037–10041.
- (114) Record, M. T., Jr.; Zhang, W.; Anderson, C. F. Analysis of effects of salts and uncharged solutes on protein and nucleic acid equilibria and processes: a practical guide to recognizing and interpreting polyelectrolyte effects, Hofmeister effects, and osmotic effects of salts. *Adv. Protein Chem.* 1998, 51, 281–353.
- (115) Anderson, C. F.; Record, M. T. Salt-nucleic acid interactions. *Annu. Rev. Phys. Chem.* **1995**, *46*, 657–700.
- (116) García-García, C.; Draper, D. E. Electrostatic interactions in a peptide–RNA complex. *J. Mol. Biol.* **2003**, *331*, 75–88.
- (117) Suresha, P. R.; Badiger, M. V.; Wolf, B. A. Polyelectrolytes in dilute solution: viscometric access to coil dimensions and salt effects. *RSC Adv.* **2015**, *5*, 27674–27681.
- (118) Izzo, D.; Cloitre, M.; Leibler, L. The viscosity of short polyelectrolyte solutions. *Soft Matter* **2014**, *10*, 1714–1722.
- (119) Jameson, D. M.; Hazlett, T. L. In *Biophysical and Biochemical Aspects of Fluorescence Spectroscopy*; Dewey, T. G., Ed.; Plenum Press: New York, 1991; pp 105–133.
- (120) Cantor, C. R.; Schimmel, P. R. Biophysical Chemistry; W.H. Freeman and Company: New York, 1980.
- (121) Berezin, M. Y.; Achilefu, S. Fluorescence lifetime measurements and biological imaging. *Chem. Rev.* **2010**, *110*, 2641–2684.
- (122) Lipari, G.; Szabo, A. Effect of librational motion on fluorescence depolarization and nuclear magnetic resonance relaxation in macromolecules and membranes. *Biophys. J.* **1980**, *30*, 489–506.
- (123) Kinosita, K.; Ikegami, A.; Kawato, S. On the wobbling-in-cone analysis of fluorescence anisotropy decay. *Biophys. J.* **1982**, *37*, 461–464
- (124) Knight, A. M.; Culviner, P. H.; Kurt-Yilmaz, N.; Zou, T.; Ozkan, S. B.; Cavagnero, S. Electrostatic effect of the ribosomal surface on nascent polypeptide dynamics. *ACS Chem. Biol.* **2013**, 8, 1195–1204.
- (125) Deckert, A.; Waudby, C. A.; Wlodarski, T.; Wentink, A. S.; Wang, X.; Kirkpatrick, J. P.; Paton, J. F. S.; Camilloni, C.; Kukic, P.; Dobson, C. M.; et al. Structural characterization of the interaction of α -synuclein nascent chains with the ribosomal surface and trigger factor. *Proc. Natl. Acad. Sci. U.S.A.* **2016**, *113*, 5012–5017.
- (126) Hoffmann, A.; Merz, F.; Rutkowska, A.; Zachmann-Brand, B.; Deuerling, E.; Bukau, B. Trigger factor forms a protective shield for nascent polypeptides at the ribosome. *J. Biol. Chem.* **2006**, *281*, 6539–6545.
- (127) Hoffmann, A.; Bukau, B.; Kramer, G. Structure and function of the molecular chaperone Trigger Factor. *Biochim. Biophys. Acta, Mol. Cell Res.* **2010**, *1803*, 650–661.
- (128) Kramer, G.; Shiber, A.; Bukau, B. Mechanisms of cotranslational maturation of newly synthesized proteins. *Annu. Rev. Biochem.* **2019**, *88*, 337–364.

- (129) Mayer, M. P.; Bukau, B. Hsp70 chaperones: cellular functions and molecular mechanism. *Cell. Mol. Life Sci.* **2005**, *62*, *670*–*684*.
- (130) Kurt, N.; Cavagnero, S. The burial of solvent-accessible surface area is a predictor of polypeptide folding and misfolding as a function of chain elongation. *J. Am. Chem. Soc.* **2005**, *127*, 15690–15691
- (131) Kurt, N.; Mounce, B. C.; Ellison, P. A.; Cavagnero, S. Residue-specific contact order and contact breadth in single-domain proteins: implications for folding as a function of chain elongation. *Biotechnol. Prog.* **2008**, *24*, 570–575.
- (132) Mounce, B. C.; Kurt, N.; Ellison, P. A.; Cavagnero, S. Nonrandom distribution of intramolecular contacts in native single-domain proteins. *Proteins* **2009**, *75*, 404–412.
- (133) Zhao, V.; Jacobs, W. M.; Shakhnovich, E. I. Effect of protein structure on evolution of cotranslational folding. *Biophys. J.* **2020**, *119*, 1123–1134.
- (134) Yaeger-Weiss, S. K.; Jennaro, T. S.; Mecha, M.; Becker, J. H.; Yang, H.; Winkler, G. L. W.; Cavagnero, S. Net charge and nonpolar content guide the identification of folded and prion proteins. *Biochemistry* **2020**, *59*, 1881–1895.
- (135) Schymkowitz, J.; Borg, J.; Stricher, F.; Nys, R.; Rousseau, F.; Serrano, L. The FoldX web server: an online force field. *Nucleic Acids Res.* **2005**, *33*, W382–W388.
- (136) Wilson, D. N.; Beckmann, R. The ribosomal tunnel as a functional environment for nascent polypeptide folding and translational stalling. *Curr. Opin. Struct. Biol.* **2011**, 21, 274–282.